

# Detailed abundance analysis of globular clusters in the Local Group.

## NGC 147, NGC 6822, and Messier 33

S. S. Larsen<sup>1</sup>, J. Brodie<sup>2</sup>, A. Wasserman<sup>2</sup>, and J. Strader<sup>3</sup>

<sup>1</sup> Department of Astrophysics/IMAPP, Radboud University, PO Box 9010, 6500 GL Nijmegen, The Netherlands  
e-mail: s.larsen@astro.ru.nl

<sup>2</sup> UCO / Lick Observatory, 1156 High Street, University of California, Santa Cruz, CA 95064, USA

<sup>3</sup> Department of Physics and Astronomy, Michigan State University, East Lansing, Michigan 48824, USA

Received September 7, 2017; accepted January 9, 2018

### ABSTRACT

**Context.** Globular clusters (GCs) are emerging as powerful tracers of the chemical composition of extragalactic stellar populations.  
**Aims.** We present new abundance measurements for eleven GCs in the Local Group galaxies NGC 147, NGC 6822, and Messier 33. These are combined with previously published observations of four GCs in the Fornax and WLM galaxies.  
**Methods.** The abundances were determined from analysis of integrated-light spectra, obtained with the HIRES spectrograph on the Keck I telescope and with UVES on the VLT. We used our analysis technique that has been developed for this purpose and tested on Milky Way GCs.  
**Results.** We find that the clusters with  $[\text{Fe}/\text{H}] < -1.5$  are all  $\alpha$ -enhanced at about the same level as Milky Way GCs. Their Na abundances are also generally enhanced relative to Milky Way halo stars, suggesting that these extragalactic GCs resemble their Milky Way counterparts in containing significant fractions of Na-rich stars. For  $[\text{Fe}/\text{H}] > -1.5$ , the GCs in M33 are also  $\alpha$ -enhanced, while the GCs that belong to dwarfs (NGC 6822 SC7 and Fornax 4) have closer to Solar-scaled  $\alpha$ -element abundances. The abundance patterns in SC7 are remarkably similar to those in the Galactic GC Ruprecht 106, including significantly sub-solar  $[\text{Na}/\text{Fe}]$  and  $[\text{Ni}/\text{Fe}]$  ratios. In NGC 147, the GCs with  $[\text{Fe}/\text{H}] < -2.0$  account for about 6% of the total luminosity of stars in the same metallicity range, a lower fraction than those previously found in the Fornax and WLM galaxies, but substantially higher than in the Milky Way halo.  
**Conclusions.** At low metallicities, the abundance patterns suggest that GCs in the Milky Way, dwarf galaxies, and M33 experienced similar enrichment histories and/or processes. At higher metallicities, the lower levels of  $\alpha$ -enhancement in the GCs found in dwarf galaxies resemble the abundance patterns observed in field stars in nearby dwarfs. Constraining the presence of multiple populations in the GCs is complicated by the lack of information about detailed abundances in field stars of the corresponding metallicities. We suggest that correlations such as  $[\text{Na}/\text{Fe}]$  vs.  $[\text{Ni}/\text{Fe}]$  may prove useful for this purpose if an accuracy of  $\sim 0.1$  dex or better can be reached for the integrated-light measurements.

**Key words.** Galaxies: star clusters - Galaxies: individual: NGC 147, NGC 6822, M 33, Fornax, WLM - Galaxies: abundances

## 1. Introduction

Characterising and understanding the chemical composition of stellar populations is a fundamentally important problem in astrophysics. While elements heavier than hydrogen and helium only account for a couple of percent of the mass of stars like the Sun (and in some stars much less), these elements are of crucial interest. They were synthesised in stellar interiors, returned to the interstellar medium, and then incorporated in subsequent generations of stars, and therefore hold important clues to the evolutionary histories of galaxies. Of course, understanding the origin of the elements is also of interest beyond a purely astrophysical context. The striking similarity between the composition of stellar photospheres and the Earth's crust was noted long ago (Payne 1925), although a detailed understanding of the synthesis of the elements in stellar interiors only started to emerge much later (e.g. Hoyle 1954).

Tinsley (1979) discussed how abundance ratios can be affected by the different time scales on which various families of elements are produced (light,  $\alpha$ -, iron-peak, and neutron-capture

elements). For example, elements that are produced predominantly in short-lived massive stars, such as oxygen, will tend to be overabundant compared to the iron-peak elements (produced in type Ia supernovae with longer-lived progenitors) in stars that formed early in the history of the Galaxy. Around the same time as Tinsley's pioneering theoretical work, observational evidence was accumulating that oxygen and calcium are indeed enhanced relative to iron in globular cluster giants (Cohen 1978; Pilachowski et al. 1980) and metal-poor halo stars (Snedden et al. 1979; Luck & Bond 1981).

It is impossible to review the extensive literature on more recent Galactic and extragalactic abundance work here. In the last two decades, a large number of studies have painted an increasingly detailed picture of the chemical composition of various Galactic components. Roughly speaking, the halo and bulge consist mainly of old,  $\alpha$ -enhanced populations, whereas young stellar populations in the disc tend to have abundance patterns similar to those seen in the Sun. Fe-peak elements (such as Cr, Sc, Ni) mostly trace the Fe abundance, while the heavy (neutron-capture) elements (e.g. Ba, Y, La, Eu) show a large scatter and an

increasing contribution from  $r$ -process dominated nucleosynthesis at low metallicities (Edvardsson et al. 1993; Fulbright 2000; Bensby et al. 2003; Reddy et al. 2003; Ishigaki et al. 2013; Bensby et al. 2014). One interesting feature that has emerged from recent high-precision measurements is a bimodal distribution of  $[\alpha/\text{Fe}]$  ratios at metallicities  $[\text{Fe}/\text{H}] \lesssim -1$ , with the less  $\alpha$ -enhanced stars having more extreme halo kinematics (Nissen & Schuster 2010; Schuster et al. 2012; Bensby et al. 2014). Many of the overall trends can be described fairly well by relatively simple models (Matteucci & Greggio 1986; Matteucci & Brocato 1990; Pagel & Tautvaisiene 1995; Chiappini et al. 2001), although chemo-dynamical models that capture more details are now also appearing (Kobayashi et al. 2006; Kobayashi & Nakasato 2011; Tissera et al. 2012). Further details can be found in several excellent reviews (McWilliam 1998; Matteucci 2001; Freeman & Bland-Hawthorn 2002; Helmi 2008).

A natural next step is to obtain abundance measurements for external galaxies and compare their chemical composition with our own Milky Way. This may help shed light on chemical enrichment in different environments and its implications for chemical evolution in the context of hierarchical galaxy assembly. For example, could the  $\alpha$ -rich and  $\alpha$ -poor halo populations described above be understood as stars formed “in situ” vs. accreted? In nearby dwarf galaxies, a considerable amount of information about detailed abundances is now available from observations of individual stars. Some differences with respect to the Galactic halo are evident: for example, the trend of  $\alpha$ -enhancement as a function of overall metallicity appears to be different in dwarf spheroidals than in the Milky Way, with the transition from significant  $\alpha$ -enhancement to more solar-like abundance ratios occurring at a lower metallicities in dwarf galaxies (Tolstoy et al. 2009). Other differences include increased  $[\text{Ba}/\text{Fe}]$  ratios and lower  $[\text{Na}/\text{Fe}]$  and  $[\text{Ni}/\text{Fe}]$  ratios in the dwarfs (Cohen & Huang 2009, 2010; Letarte et al. 2010; Lemasle et al. 2014; Hendricks et al. 2016). The reasons for these differences may include differences in the time scales for chemical enrichment, galactic winds, and variations in the stellar initial mass function (Lanfranchi et al. 2006; Romano & Starkenburg 2013; McWilliam et al. 2013; Homma et al. 2015; Vincenzo et al. 2015).

In all but the closest of our neighbouring galaxies, individual stars are generally too faint for detailed abundance studies, especially for old stellar populations. Observations of early-type galaxies in integrated light have provided interesting constraints on  $\alpha$ -enrichment, which tends to increase with velocity dispersion (Worthey et al. 1992; Kuntschner 2000; Trager et al. 2000; Thomas et al. 2005) and even on individual abundance ratios (Conroy et al. 2014). However, a limitation of this type of work is that it only provides luminosity-weighted mean abundances, which are usually dominated by the more metal-rich populations. In order to access populations that only account for a minor fraction of the light, other methods are required. Here, *globular clusters* (GCs) offer an attractive tracer of sub-populations within external galaxies as they are far brighter than individual red giants. In particular, the metal-poor components in galaxies usually account for only a small fraction of the stars, but often have large numbers of GCs associated with them.

A number of recent studies have used integrated-light spectroscopy at high resolution to measure chemical abundances of extragalactic GCs. In M31, as in the Milky Way, such measurements show that GCs generally have enhanced  $\alpha$ -element abundances, although some clusters show abundance patterns that more closely resemble those seen in dwarf galaxies (Colucci et al. 2009, 2014; Sakari et al. 2015). A similar case in the

Milky Way is Ruprecht 106, for which an accretion origin has been suggested (Villanova et al. 2013). In a pilot study we used integrated-light spectroscopy to determine chemical abundances for three globular clusters (Fornax 3, Fornax 4, and Fornax 5) in the Fornax dwarf spheroidal galaxy. We confirmed that Fornax 3 and Fornax 5 are relatively metal-poor compared to typical Milky Way and M31 halo GCs (both having  $[\text{Fe}/\text{H}] < -2$ ), while Fornax 4 has  $[\text{Fe}/\text{H}] = -1.4$ . The  $[\alpha/\text{Fe}]$  ratios ( $[\text{Ca}/\text{Fe}]$ ,  $[\text{Ti}/\text{Fe}]$ ) of Fornax 3 and Fornax 5 were found to be enhanced, although possibly slightly less so than in Milky Way GCs, while the  $[\alpha/\text{Fe}]$  ratio in Fornax 4 was only slightly elevated compared to Solar-scaled abundance patterns (Larsen et al. 2012a, hereafter L12). This is in agreement with the trends observed in field stars in dwarf galaxies. Subsequently we applied our technique to the lone GC in the Wolf-Lundmark-Melotte (WLM) galaxy, which was also found to be metal-poor ( $[\text{Fe}/\text{H}] \approx -2$ ) and with chemical abundance patterns similar to those in Milky Way GCs (Larsen et al. 2014a, L14). We note that similar techniques have also been applied to *young* star clusters in external star-forming galaxies (Larsen et al. 2006, 2008; Gazak et al. 2014; Lardo et al. 2015; Cabrera-Ziri et al. 2016; Hernandez et al. 2017, 2018) where they provide a welcome alternative to more traditional tracers of the chemical composition of young stellar populations (e.g.,  $\text{H II}$  regions).

A unique aspect of GCs is the abundance spreads that affect the light elements within the clusters (Gratton et al. 2012). In nearly all Galactic GCs studied to date, about half of the stars have elevated abundances of certain elements (He, N, Na, and sometimes Al) while others are depleted (C, O, and sometimes Mg). Evidently, this needs to be kept in mind when using GCs as probes of stellar populations. On the other hand, integrated-light observations have the potential to constrain the occurrence of multiple populations in extragalactic environments. Indeed, the integrated-light abundances of elements like Na and Mg suggest that multiple populations are common also in extragalactic GCs (Larsen et al. 2014a; Colucci et al. 2014; Sakari et al. 2015).

Here we present new abundance measurements for GCs in three additional Local Group galaxies: NGC 147, NGC 6822, and M33. We use the same measurement technique that we have previously used for GCs in Fornax and WLM. Additional tests were described in Larsen et al. (2017, hereafter L17) where we compared integrated-light observations of seven Galactic GCs, spanning a broad range of metallicities, with literature data for individual stars in the clusters. In the following we briefly summarise previous work on chemical abundances in the three galaxies, concentrating on old stellar populations.

It is well-established that M33 has a metal-poor halo which is traced by red giant branch (RGB) stars (Brooks et al. 2004) and RR Lyrae variables (Sarajedini et al. 2006), as well as GCs (Christian & Schommer 1982; Sarajedini et al. 1998, 2000). These tracers all indicate an average metallicity of around  $[\text{Fe}/\text{H}] = -1.3$ , but there is currently little information available about the detailed chemical composition of the M33 halo. From medium-dispersion spectroscopy of 15 GCs, Sharina et al. (2010) found a range of  $[\alpha/\text{Fe}]$  values between 0 and +0.5. A significant age spread among the M33 halo GCs has been suggested based on their horizontal branch (HB) morphologies (Sarajedini et al. 1998), and it would be interesting to investigate whether there is corresponding evidence of an extended formation history in the GC abundances. For example, one might expect the  $[\alpha/\text{Fe}]$  ratios to be closer to the Solar ratio if the clusters formed out of material that had time to become significantly enriched by type Ia SN ejecta.

NGC 147 is a dE companion of M31 which is now known to host 10 old GCs, of which six have been discovered relatively recently (Sharina & Davoust 2009; Veljanoski et al. 2013). The metallicity distribution of the field stars in NGC 147 is quite broad with a peak at  $[\text{Fe}/\text{H}] = -0.5$  (Ho et al. 2014). In contrast, at least 7 out of the 10 GCs appear to have metallicities below  $[\text{Fe}/\text{H}] = -1.5$  (Veljanoski et al. 2013). NGC 147 thus exhibits the same offset between the GC and field star metallicity distributions that is observed in many other galaxies, including dwarf galaxies such as Fornax and WLM (Larsen et al. 2012b, 2014a; Lamers et al. 2017). Vargas et al. (2014) estimated average  $[\alpha/\text{Fe}]$  ratios for RGB stars in NGC 147 and found them to be generally super-solar, although only one star had a metallicity below  $[\text{Fe}/\text{H}] = -1.5$ .

NGC 6822 (“Barnard’s galaxy”) is a relatively isolated (within the Local Group) dwarf irregular galaxy, located at a distance of about 479 kpc (Feast et al. 2012). Its HII regions have long been known to be more metal-poor than those in the Milky Way (Peimbert & Spinrad 1970). Modern studies based on various methods all agree on a metallicity close to  $[\text{Fe}/\text{H}] = -0.5$  for the young stellar population in NGC 6822: for HII regions, Lee et al. (2006) found  $[\text{O}/\text{H}] = -0.55 \pm 0.10$ , while Venn et al. (2001) found  $[\text{Fe}/\text{H}] = -0.49 \pm 0.22$  (blue supergiants) and Patrick et al. (2015) measured  $[\text{Fe}/\text{H}] = -0.52 \pm 0.21$  (red supergiants). Information about older populations is more scarce, but Swan et al. (2016) found an average metallicity of  $\langle [\text{Fe}/\text{H}] \rangle = -0.84 \pm 0.04$  with a dispersion of 0.31 dex from Ca II IR triplet measurements of RGB stars. These authors also give a listing of other metallicity estimates. Until just a few years ago, NGC 6822 was thought to host only a single old GC, Hubble VII (Hubble 1925). From integrated-light spectroscopy of Hubble VII, Colucci & Bernstein (2011) found  $[\text{Fe}/\text{H}] = -1.61 \pm 0.02$ ,  $[\text{Ca}/\text{Fe}] = +0.01 \pm 0.07$  and  $[\text{Ba}/\text{Fe}] = +0.22 \pm 0.13$ . Apart from this measurement, little is known about the detailed chemical composition of old stellar populations in NGC 6822. In recent years, wide-field imaging has uncovered several previously uncatalogued GCs around NGC 6822 and the total now stands at 8 (Hwang et al. 2011; Huxor et al. 2013), several of which are compact and bright enough that good integrated-light spectra can be obtained in a modest amount of observing time with a 10 m class telescope.

## 2. Observations

New observations of globular clusters in NGC 147 and NGC 6822 were obtained with the HIRES spectrograph (Vogt et al. 1994) on the Keck I telescope on 5 Oct 2015 and 25 Sep 2016. The observations on the night of 5 Oct 2015 were affected by clouds and high humidity (two nights had been scheduled for this run, of which the first was completely lost), whereas conditions during the Sep 2016 run were excellent. The clusters were selected from Veljanoski et al. (2013) and Veljanoski et al. (2015), concentrating primarily on the brighter, more compact objects. A log of the observations is given in Table 1. We used the C5 decker in HIRES, which provides a slit length of  $7''$  and a slit width of  $1''.148$ , corresponding to a spectral resolving power of  $R \approx 37\,000$ . The detectors were binned by 2 pixels in the spatial direction, with a resulting spatial scale of  $0''.24$  per (binned) pixel.

The clusters NGC 147-Hodge II and NGC 6822-SC6 each has a relatively bright star at  $8''$ – $10''$  from the cluster centre. Although this is, in both cases, well beyond the half-length of the HIRES slit, we chose the slit position angle so as to avoid any potential light from these stars. For all other HIRES observations

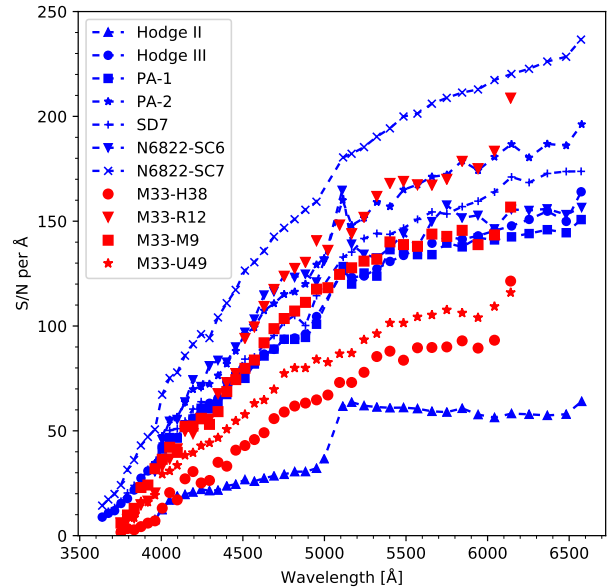


**Fig. 1.** Median signal-to-noise ratio per spectral order for the GCs in NGC 147, NGC 6822, and M33.

used in this paper, the slit was aligned vertically. This implies that the slit position angle on the sky changed during the exposures, typically by  $5^\circ$ – $20^\circ$ , depending on the zenith angle. The background level measured at the ends of the slit thus represents an average over many position angles and is naturally smoothed over any small-scale fluctuations that might be caused, for example, by fainter stars in the vicinity of the clusters.

The HIRES echellogram is recorded onto three separate detectors, which introduces small gaps in the wavelength coverage. The wavelength windows affected by these gaps can be chosen by adjusting the tilt of the echelle- and cross disperser gratings. We set the grating angles so as to have the gaps occur at  $4990\text{ Å}$ – $5090\text{ Å}$  and at  $6600\text{ Å}$ – $6690\text{ Å}$ , which minimised the loss of important spectral diagnostics. Of the features measured in L17, we only miss the Sc II line at  $5031\text{ Å}$  and several Ti lines near  $5000\text{ Å}$ . Apart from the gaps, the wavelength coverage is continuous from  $3900\text{ Å}$  to about  $6300\text{ Å}$  beyond which the ends of the echelle orders fall off the edges of the detectors. The spectra extend to about  $8100\text{ Å}$  but in our analysis we concentrate on the spectral regions that we have used in our previous studies, i.e.,  $4200\text{ Å}$ – $6200\text{ Å}$ .

We also include older HIRES observations of four GCs in M33. The spectra are the same as those used by Larsen et al. (2002) to measure the internal velocity dispersions of the clusters and derive dynamical masses, and we refer to that paper for details about the observations and data reduction. These spectra were obtained on 24–25 October 1998. The detector then in use at HIRES covered the wavelength range  $3730\text{ Å}$ – $6170\text{ Å}$ , distributed over 38 echelle orders with some gaps in the wavelength coverage between the orders at wavelengths longer than  $\sim 5000\text{ Å}$ . Since the original purpose of these observations was to measure velocity dispersions, a narrower slit ( $0''.725$ ) was used, with a correspondingly higher resolving power of  $R \approx 54\,000$ . The slit used for these observations had a length of  $5''$ . The total integration times were 3.5–4.5 hrs, divided into 7–9 sub-exposures per cluster.

**Table 1.** Log of observations.

Cluster	V mag	Date	T(exp) s	$v_{\text{hel}}^a$ km s <sup>-1</sup>	$\sigma_{\text{ID}}^b$ km s <sup>-1</sup>
M33 R12	16.5 <sup>1</sup>	24 Oct 1998	7 × 1800 s	-218	6.5
M33 U49	16.0 <sup>1</sup>	24 Oct 1998	8 × 1800 s	-150	7.6
M33 H38	17.4 <sup>1</sup>	25 Oct 1998	7 × 1800 s	-241	5.5
M33 M9	17.1 <sup>1</sup>	25 Oct 1998	9 × 1800 s	-249	5.9
NGC 147 HIII	16.6 <sup>2</sup>	5 Oct 2015	4 × 1800 s	-197	6.6
NGC 147 HII	18.1 <sup>2</sup>	25 Sep 2016	4 × 1800 s	-207	2.5
NGC 147 SD7	17.0 <sup>2</sup>	5 Oct 2015	4 × 1800 s	-197	5.3
NGC 147 PA-1	17.0 <sup>2</sup>	5 Oct 2015	1800 s + 865 s	-221	6.1
		25 Sep 2016	2 × 1800 s		
NGC 147 PA-2	17.4 <sup>2</sup>	25 Sep 2016	5 × 1800 s	-221	6.1
NGC 6822 SC6	16.0 <sup>3</sup>	25 Sep 2016	2 × 1800 s	-5	8.7
NGC 6822 SC7	15.4 <sup>3</sup>	5 Oct 2015	1800 s + 1139 s	-39	9.2

**Notes.** (a) Heliocentric radial velocity. (b) One-dimensional velocity dispersion, corrected for instrumental resolution.

**References.** Integrated visual magnitudes: (1) Larsen et al. (2002); (2) Veljanoski et al. (2013); (3) Veljanoski et al. (2015).

All HIRES spectra were reduced with the MAKEE (MAuna Kea Echelle Extraction) package<sup>1</sup> written by T. Barlow. MAKEE is designed to carry out all reduction steps with minimal user interaction, from bias subtraction and flat-fielding to tracing of the spectral orders, wavelength calibration, sky subtraction, and extraction of the final one-dimensional spectra using optimal weighting. Owing to the relatively short slit, definition of the sky regions involves a compromise between maximising the number of pixels used for the sky level determination and those used for extraction of the object spectrum. Also, especially for observations at high airmass, differential atmospheric refraction causes the clusters to appear off-center along the slit at bluer wavelengths. Hence, MAKEE determines the background regions individually for each echelle order based on the location of the centroid of the trace along the slit and the width of the object profile. The exact criteria controlling the sky subtraction and extraction are defined in a configuration file, where in most cases we used the default configuration file for HIRES provided with MAKEE. Here, the spacing between the object and sky regions is set to one pixel and the *minimum* amount of sky on either side of the object is also one pixel. In practice, 2–5 binned pixels were typically used for sky determination on either side of the trace. In the absence of strong sky lines, MAKEE further averages the sky background over five adjacent pixels along the dispersion direction. The background subtracted from the object spectrum is then determined from a linear fit to the sky regions on either side of the trace (if the ratio of the sky areas is less than 2:1) or from a simple average of the sky pixels otherwise. For NGC 147-Hodge II, which is the faintest of our targets, we customised the configuration file to make MAKEE use at least five pixels on either side of the trace of the cluster spectra to determine the sky background level. As a check we also reduced some of the spectra with the IDL HIRES Redux package written by J. Prochaska. The results were found to be very similar to those obtained with MAKEE.

The one-dimensional spectra extracted from each individual exposure were combined using a sigma-clipping algorithm to reject outlying pixels (e.g., due to cosmic ray hits), and the signal-to-noise (S/N) ratio of the combined spectra was estimated from the variance at each pixel. In Fig. 1 we show the S/N curves

for our HIRES observations. Note that the S/N is given per Å; the S/N per pixel is thus lower by a factor  $\sqrt{\Delta\lambda/\text{Å}}$  where  $\Delta\lambda$  is the wavelength step per pixel, ranging from  $\Delta\lambda = 0.018 \text{ Å}$  at 4200 Å to  $\Delta\lambda = 0.027 \text{ Å}$  at 6200 Å. For most clusters we reach a S/N > 100 per Å at 5000 Å.

In addition to the HIRES observations, we include our previously published VLT/UVES spectra of GCs in the Fornax and WLM galaxies (Larsen et al. 2012a, 2014a) and we refer to our previous papers for details on the observational strategy and data reduction. The Fornax GCs have half-light radii of several arcsec and for these clusters the UVES slit was scanned across the clusters in the north-south and east-west directions to sample the integrated light well. The science scans were bracketed by sky scans to facilitate sky subtraction. Basic reduction of the UVES data was carried out using the standard ESO pipeline (see L12 and L14 for details). For homogeneity, we have reanalysed these data using the exact same procedures as the HIRES data, but the differences with respect to our previously published results are generally very minor.

### 3. Analysis

Abundances were measured by means of our full spectral fitting technique, which has been described in detail and tested in our previous papers (L12, L14, L17). We continued to use the line list of Castelli & Hubrig (2004) with the modifications discussed in L17. We have updated the Mg oscillator strengths using data from the 18 Feb 2016 version of the Kurucz line list<sup>2</sup>, which are identical to those in the NIST database (Kramida et al. 2013). As discussed in L17, these oscillator strengths agree better with those used by other recent studies. We have revised our procedure for selecting regions used to match the scaling of observed and model spectra. As noted in L14, using all available pixels when determining this scaling may lead to biased results, because model spectra are never a perfect match to real data. We have previously used the spectrum of Arcturus to identify “continuum” regions, free of strong lines, to be used for the scaling. Here we made use of the spectrum of 47 Tuc (NGC 104) analysed in L17, and selected regions where the NGC 104 spectrum and our best-fitting model spectrum agreed to within better

<sup>1</sup> Available at <http://www.astro.caltech.edu/~tb/makee/>

<sup>2</sup> <http://kurucz.harvard.edu/linelists.html>

**Table 2.** Isochrone parameters and horizontal branches used for modelling of integrated-light spectra.

Object	Age	[Fe/H]	[ $\alpha$ /Fe]	HB from
NGC 147 HII	13	-1.5	+0.4	NGC 6254
NGC 147 HIII	13	-2.5	+0.4	NGC 7078
NGC 147 SD7	13	-2.0	+0.4	NGC 6779
NGC 147 PA-1	13	-2.3	+0.4	NGC 7078
NGC 147 PA-2	13	-2.1	+0.4	NGC 6779
NGC 6822 SC6	13	-1.8	+0.4	NGC 6093
NGC 6822 SC7	13	-1.3	0.0	NGC 362
M33 H38	10	-1.2	+0.4	NGC 362
M33 M9	13	-1.8	+0.4	NGC 6093
M33 R12	10	-0.8	+0.4	NGC 362
M33 U49	10	-1.4	+0.4	NGC 362
WLM GC	13	-2.0	+0.2	NGC 6779
Fornax 3		Empirical CMD		
Fornax 4		Empirical CMD		
Fornax 5		Empirical CMD		

**Notes.** Isochrone ages (2nd column) are in Gyr. The last column indicates the names of the globular clusters from which horizontal branches were adopted.

than 2%. With this modification, we used about 66% of the pixels for overall scaling, compared with about 32% (in the range  $4200 < \lambda/\text{\AA} < 6200$ ) with the selection based on the Arcturus spectrum.

To build our integrated-light model spectra, we used input Hertzsprung-Russell diagrams (HRDs) based on theoretical isochrones from the Dartmouth group for stellar evolutionary phases up to the tip of the RGB (Dotter et al. 2007). We generally assumed ages of 13 Gyr, while the metallicities and  $\alpha$ -enrichment of the isochrones were chosen to match the values derived from fits. This procedure typically converged after 1–2 iterations. As in our previous work, the isochrones were populated according to a stellar mass function of the Salpeter (1955) form,  $dN/dM \propto M^{-2.35}$ , down to a lower absolute magnitude limit of  $M_V = +9$ . The isochrones were combined with empirical data for the horizontal branches (HBs) of Galactic GCs (Sarajedini et al. 2007) with metallicities roughly matching those of the isochrones. As noted by Sarajedini et al. (1998), some of the GCs in M33 have unusually red horizontal branches for their metallicities, which may be an indication that they are somewhat younger than their Galactic counterparts, although the mass-to-light ratios are similar to those of Galactic GCs (Larsen et al. 2002). For these clusters we assumed ages of 10 Gyr and we used the (red) HB of the globular cluster NGC 362. For the globular clusters in the Fornax dSph we used the same input HRDs, based on HST colour-magnitude diagrams, as in L12. Table 2 summarises the isochrone parameters and HB data used for each cluster.

In general, abundances of Na, Mg, Ca, Sc, Ti, Cr, Mn, and Ba were determined using the same spectral bins as in our previous work. However, since the HIRES reduction pipelines do not merge the echelle orders to a single spectrum, we determined the Fe abundances by fitting each echelle order separately, rather than in 200 Å bins as was done for our UVES observations. A new addition is that we also included 14 bins containing Ni lines. In a few cases, the edges of the spectral bins had to be adjusted in order to stay within one echelle order. For the M33 GC spectra, a few features fell in the gaps between echelle orders, allowing us to measure only three Mg lines instead of the five we mea-

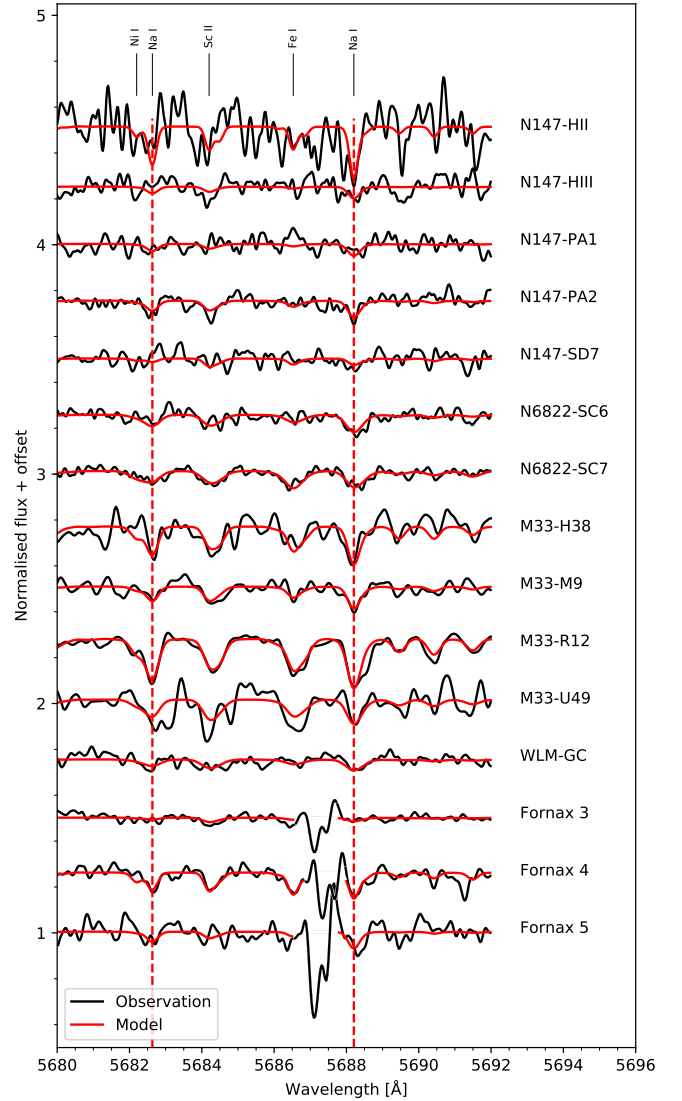


**Fig. 2.** Fits to the Na I doublet at 5683/5688 Å (red dashed lines). Note that the bad pixels near 5687 Å in the Fornax spectra have been excluded from the fits. Both models and data have been smoothed using a Gaussian kernel with  $\sigma = 2$  pixels.

sured for the other clusters. For the Fornax spectra we now include measurements of Na, which was omitted in L12 because of a block of bad pixels near the 5683/5688 Å doublet. However, the 6154/6161 Å lines are strong enough to measure in the Fornax 4 spectrum, and for this spectrum we found the two Na I doublets to give  $[\text{Na}/\text{Fe}] = -0.177 \pm 0.045$  (5683/5688 Å) and  $[\text{Na}/\text{Fe}] = -0.258 \pm 0.120$  (6154/6161 Å), i.e., consistent within the measurement errors. This is also in agreement with our analysis in L17, which showed that the spectral synthesis technique performs well even for the weaker and more blended Na I lines at 6154/6161 Å. Hence, we now feel sufficiently confident about these measurements that we choose to quote Na abundances also for the Fornax GCs. Fig. 2 shows the fits to the Na I 5683/5688 Å doublet for all clusters studied here and it can be seen that the bad pixels in the Fornax spectra (which are masked out in the fits) are located just bluewards of the 5688 Å line. Fig. 3 shows additional example fits to the spectral region near 5600 Å, which contains a number of Ca I lines.



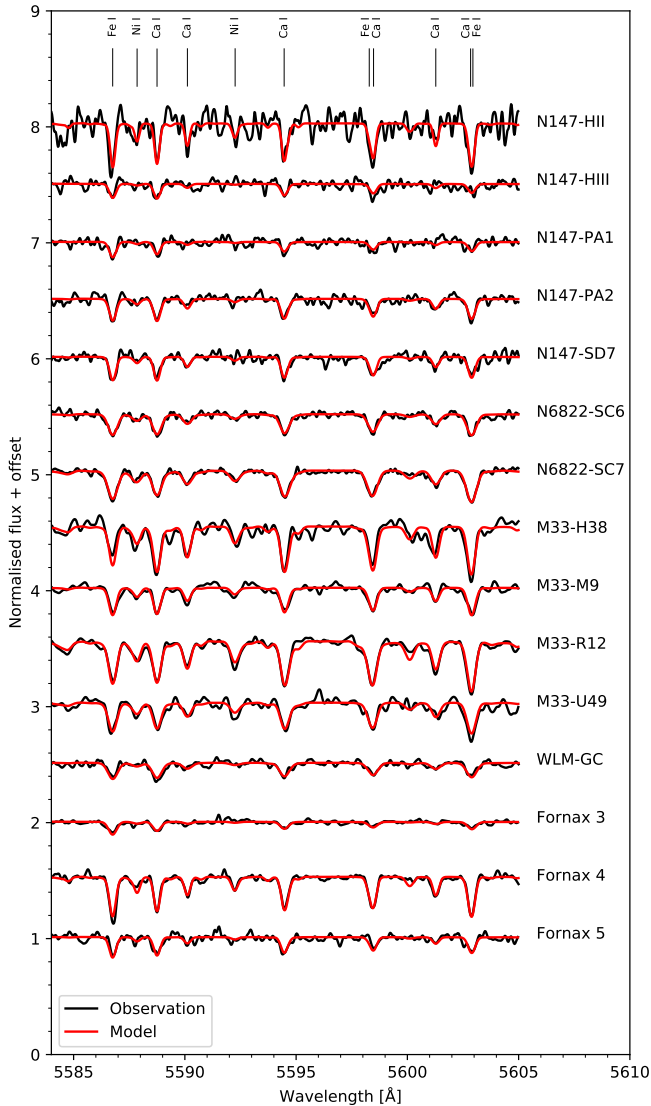


**Fig. 3.** Fits to the spectral region near 5600 Å. Both models and data have been smoothed using a Gaussian kernel with  $\sigma = 2$  pixels.

We include in Table 1 the heliocentric radial velocities ( $v_{\text{hel}}$ ) and line-of-sight velocity dispersions ( $\sigma_{\text{1D}}$ ) obtained as part of our analysis. For the velocity dispersions, we have subtracted the instrumental resolution in quadrature ( $\sigma_{\text{inst}} = 2.4 \text{ km s}^{-1}$  for the 1998 observations,  $\sigma_{\text{inst}} = 3.4 \text{ km s}^{-1}$  otherwise). The errors on the radial velocities are dominated by systematics, but are probably accurate to within  $\sim 1 \text{ km s}^{-1}$  (L17). For Hodge III, Sharina & Davoust (2009) quoted a velocity of  $-118 \pm 30 \text{ km s}^{-1}$ , which differs substantially from the systemic velocity of NGC 147 ( $-193.1 \pm 0.8 \text{ km s}^{-1}$ ; Geha et al. 2010). Our measurement ( $-197 \text{ km s}^{-1}$ ) is much closer to the velocity of NGC 147. For the other clusters in NGC 147 and NGC 6822, our new measurements agree well with previous literature data (Sharina & Davoust 2009; Veljanoski et al. 2013, 2015). For U49 and R12 in M33, the radial velocities derived from our analysis agree well (to within about  $1 \text{ km s}^{-1}$ ) with those found by Larsen et al. (2002) from cross-correlation with the star HD 1918. However, for H38 and M9 the velocities found here are  $47 \text{ km s}^{-1}$  lower (more negative) than those found by Larsen et al. (2002). This is probably due to a misidentification of the template star: U49 and R12 were observed on the first night of the 1998 observ-

**Table 3.** Sensitivity to SSP modelling assumptions for M33-U49.

	$t = 13 \text{ Gyr}$	NGC 5272 HB
$\Delta[\text{Fe}/\text{H}]$	-0.063	+0.058
$\Delta[\text{Na}/\text{Fe}]$	+0.034	-0.036
$\Delta[\text{Mg}/\text{Fe}]$	-0.046	+0.125
$\Delta[\text{Ca}/\text{Fe}]$	+0.011	-0.070
$\Delta[\text{Sc}/\text{Fe}]$	+0.034	-0.025
$\Delta[\text{Ti}/\text{Fe}]$	+0.008	+0.052
$\Delta[\text{Cr}/\text{Fe}]$	+0.019	-0.026
$\Delta[\text{Mn}/\text{Fe}]$	+0.013	-0.001
$\Delta[\text{Ni}/\text{Fe}]$	+0.004	+0.008
$\Delta[\text{Ba}/\text{Fe}]$	-0.008	+0.061

**Notes.** Differences are listed with respect to the “standard” abundances derived for  $t = 10 \text{ Gyr}$  and the NGC 362 horizontal branch.

ing run, apparently together with the correct star. The two other clusters were observed the following night, and inspection of the original FITS headers for the template star observations reveals that the telescope was pointed at another star about  $1'$  from the position of HD 1918. We have verified by cross-correlating the two template spectra that their radial velocities do indeed differ by  $47 \text{ km s}^{-1}$ . Apparently the star observed on the second night was not HD 1918 but another star. Our new radial velocities for R12, U49, and H38 agree with those measured by Chandar et al. (2002) within the errors quoted in that study ( $10\text{--}20 \text{ km s}^{-1}$ ), while our velocity for M9 is about  $36 \text{ km s}^{-1}$  more negative. The velocity dispersions for the M33 GCs in Table 1 agree with the “direct fit” values derived by Larsen et al. (2002) within about  $0.5 \text{ km s}^{-1}$ , with no significant differences between clusters observed on the first and second night. This suggests that the template star misidentification does not significantly influence the results in that paper (apart from the radial velocities).

### 3.1. Age and horizontal branch morphology

In our previous papers (L12, L14, L17) we have assessed many of the uncertainties and systematics related to particular choices made in the modelling. Given that the horizontal branch morphology is uncertain for many of the clusters studied here, we carried out an additional set of fits for one of the clusters in M33 (U49), using the blue horizontal branch of the Galactic GC NGC 5272 instead of the red horizontal branch of NGC 362. The resulting changes in the abundance ratios are listed in Table 3. To assess the effect of age uncertainties, we also list abundance changes for an assumed age of 13 Gyr instead of 10 Gyr. The differences are generally small (less than 0.1 dex). Changing the HB morphology has the largest effect on the  $[\text{Mg}/\text{Fe}]$  and  $[\text{Ca}/\text{Fe}]$  ratios (which increase by 0.13 dex and decrease by 0.07 dex, respectively) and also increases the iron abundance by 0.06 dex. Changing the age decreases the iron abundance by 0.06 dex, but hardly affects most abundance ratios.

## 4. Results

The individual abundance measurements for each spectral bin are given in Tables A.1–A.15. Bins for which the spectral fitting procedure failed to converge to a value within  $-1 < [\text{X}/\text{Fe}] < +1$  (typically because of low S/N) are marked as “...” and in some cases only upper limits could be determined. The average abundance measurements are listed in Table 4. For each cluster, we give the weighted mean of the measurements for each individual

**Table 4.** Abundance measurements.

	[Fe/H] rms <sub>w</sub> (N)	[Na/Fe] rms <sub>w</sub> (N)	[Mg/Fe] rms <sub>w</sub> (N)	[Ca/Fe] rms <sub>w</sub> (N)	[Sc/Fe] rms <sub>w</sub> (N)	[Ti/Fe] rms <sub>w</sub> (N)	[Cr/Fe] rms <sub>w</sub> (N)	[Mn/Fe] rms <sub>w</sub> (N)	[Ni/Fe] rms <sub>w</sub> (N)	[Ba/Fe] rms <sub>w</sub> (N)
NGC 147 HII	-1.541	+0.398	+0.254	+0.260	+0.147	+0.316	-0.111	-0.164	+0.248	-0.203
	0.279 (24)	0.085 <sup>a</sup> (1)	0.206 (4)	0.215 (6)	0.269 (5)	0.153 (6)	0.230 (8)	0.269 (2)	0.342 (11)	0.427 (3)
NGC 147 HIII	-2.480	+0.648	+0.190	+0.447	+0.243	+0.509	-0.198	+0.200	-0.027	-0.255
	0.154 (25)	0.091 <sup>a</sup> (1)	0.150 (4)	0.136 (6)	0.407 (5)	0.198 (8)	0.288 (7)	0.299 (2)	0.455 (5)	0.065 (4)
NGC 147 PA-1	-2.370	+0.552	+0.298	+0.227	+0.023	+0.372	+0.002	+0.032	-0.276	+0.172
	0.133 (22)	0.146 <sup>a</sup> (1)	0.177 (5)	0.222 (8)	0.389 (5)	0.159 (9)	0.353 (10)	0.080 (1)	0.300 (4)	0.137 (4)
NGC 147 PA-2	-2.011	+0.343	+0.395	+0.390	+0.136	+0.384	+0.017	-0.244	+0.075	+0.408
	0.093 (27)	0.085 <sup>a</sup> (1)	0.161 (5)	0.134 (8)	0.232 (6)	0.129 (9)	0.182 (10)	0.098 (2)	0.226 (11)	0.064 (4)
NGC 147 SD7	-2.057	-0.192	+0.532	+0.364	+0.002	+0.432	+0.048	-0.409	+0.195	+0.432
	0.111 (26)	0.166 <sup>a</sup> (1)	0.396 (5)	0.137 (8)	0.303 (6)	0.146 (10)	0.257 (11)	0.027 (2)	0.333 (12)	0.341 (4)
NGC 6822 SC6	-1.822	+0.284	+0.295	+0.228	+0.110	+0.290	-0.049	-0.426	-0.058	+0.408
	0.078 (27)	0.090 <sup>a</sup> (1)	0.240 (6)	0.170 (8)	0.158 (7)	0.091 (9)	0.123 (11)	0.068 (2)	0.203 (13)	0.107 (4)
NGC 6822 SC7	-1.271	-0.366	-0.180	+0.042	-0.318	+0.013	-0.112	-0.388	-0.137	+0.283
	0.092 (26)	0.070 <sup>a</sup> (1)	0.208 (5)	0.141 (8)	0.118 (7)	0.128 (10)	0.098 (11)	0.020 (2)	0.236 (14)	0.044 (4)
M33 H38	-1.176	-0.020	+0.016	+0.293	-0.024	+0.367	+0.016	-0.571	+0.189	+0.657
	0.215 (23)	0.096 <sup>a</sup> (1)	0.409 (2)	0.355 (8)	0.108 (3)	0.383 (12)	0.310 (8)	0.178 (2)	0.346 (12)	0.129 (4)
M33 M9	-1.739	+0.207	-0.030	+0.263	+0.105	+0.351	-0.037	-0.378	+0.069	+0.588
	0.101 (26)	0.081 <sup>a</sup> (1)	0.165 (3)	0.177 (9)	0.235 (6)	0.154 (12)	0.110 (9)	0.115 (2)	0.268 (12)	0.130 (3)
M33 R12	-0.942	+0.098	+0.206	+0.285	+0.087	+0.261	+0.026	-0.215	+0.068	+0.395
	0.079 (26)	0.041 <sup>a</sup> (1)	0.083 (3)	0.144 (9)	0.141 (6)	0.146 (12)	0.157 (11)	0.067 (2)	0.192 (13)	0.166 (4)
M33 U49	-1.446	+0.057	+0.266	+0.219	+0.257	+0.380	+0.109	-0.023	+0.145	+0.544
	0.133 (26)	0.115 <sup>a</sup> (1)	0.154 (3)	0.337 (8)	0.230 (5)	0.246 (11)	0.290 (10)	0.137 (2)	0.379 (10)	0.407 (3)
WLM GC	-1.947	+0.217	+0.057	+0.236	+0.213	+0.177	-0.113	-0.474	-0.059	+0.099
	0.088 (10)	0.141 <sup>a</sup> (1)	0.129 (5)	0.121 (6)	0.181 (6)	0.164 (9)	0.185 (6)	0.083 (2)	0.196 (12)	0.169 (4)
Fornax 3	-2.353	+0.013	-0.014	+0.239	+0.185	+0.311	-0.189	-0.466	-0.016	+0.554
	0.066 (10)	0.171 <sup>a</sup> (1)	0.163 (5)	0.157 (8)	0.183 (6)	0.101 (9)	0.095 (6)	0.133 (2)	0.259 (13)	0.089 (3)
Fornax 4	-1.374	-0.177	-0.014	+0.073	-0.077	+0.124	-0.089	-0.365	-0.179	+0.272
	0.052 (10)	0.045 <sup>a</sup> (1)	0.189 (5)	0.130 (8)	0.095 (6)	0.094 (9)	0.093 (6)	0.053 (2)	0.155 (15)	0.060 (4)
Fornax 5	-2.125	+0.484	+0.205	+0.273	+0.012	+0.267	+0.059	-0.367	+0.049	-0.005
	0.076 (10)	0.096 <sup>a</sup> (1)	0.154 (5)	0.174 (8)	0.263 (6)	0.088 (9)	0.181 (6)	0.066 (1)	0.223 (14)	0.127 (4)

**Notes.** For each cluster, the first line gives the average abundance ratio and the second line gives the weighted rms and number of individual measurements. (a): For [Na/Fe] we list the errors on the individual measurements of the doublet at 5683/5688 Å.

bin, as well as the weighted r.m.s. (rms<sub>w</sub>, calculated as in L17) and number of measurements  $N$ . The weights were assigned as described in L17, i.e. a “floor” of 0.01 dex has been added in quadrature to the formal errors on the individual measurements. Bins for which the spectral fitting procedure failed to converge, or only upper limits were obtained, have been excluded. For Na, Table 4 only uses the values based on the 5683/5688 Å doublet, although Tables A.1–A.15 also list measurements of the weaker 6154/6161 Å lines (that typically have large errors). As found in L17, the two Na I doublets generally yield consistent abundances within the errors.

Our new measurements for the Fornax and WLM clusters generally differ little with respect to our previously published values. The largest differences are for Ba, with our new analysis yielding [Ba/Fe] values that are lower by 0.2–0.3 dex. As discussed in L17, this is due to a combination of updated  $\log g f$  values and the fact that we now assume an  $r$ -process dominated isotopic mixture for Ba (effectively making hyperfine structure more important). The [Mg/Fe] ratios have increased systematically by on average 0.04 dex, which can again be attributed to updated  $\log g f$  values (L17). This brings the Mg abundances into closer agreement with the other alpha-elements (Ca, Ti), although [Mg/Fe] is still significantly lower than the [Ca/Fe] and [Ti/Fe] ratios for a few clusters. We discuss these clusters in more detail below (Sect. 4.3.1). For other abundances ratios, the systematic differences between our previous and current analyses are less than 0.02 dex.

#### 4.1. Metallicities: comparisons with previous work

In Table 5 we list previous estimates of the cluster metallicities based on various techniques. In most cases, these previous studies have not measured [Fe/H] directly, but have estimated it based on line index measurements, broad-band colours, or RGB slope, as indicated in the Table. For Hodge II and SD7 in NGC 147 we quote the [Fe/H] values from Sharina & Davoust (2009), which were obtained using the STECKMAP method (Ocvirk et al. 2006). The authors do not quote errors for these values, but for overall metallicities,  $[Z/H]$  (determined via line indices), they quote uncertainties of typically  $\pm 0.2$  dex.

In NGC 147, the overall ranking of the cluster metallicities according to the literature studies agrees well with our measurements: Hodge II is consistently found to be the most metal-rich of the clusters, followed by PA-2 and SD7, while Hodge III and PA-1 are the most metal-poor. Indeed, our measurement of  $[Fe/H] = -2.5$  for Hodge III places this cluster among the most metal-poor GCs known, with a metallicity similar to or slightly below those of the most metal-poor GCs in the Milky Way such as M15, M30, M92, and NGC 5053 (Harris 1996), and comparable to Fornax 1, the most metal-poor GC in the Fornax dwarf galaxy (Letarte et al. 2006; Larsen et al. 2014b). For SC6 and SC7 in NGC 6822 there are no previous spectroscopic metallicity determinations, but Veljanoski et al. (2015) estimated metallicities from broad-band colours using both the empirical colour-metallicity relation of Kissler-Patig et al. (2002) and comparison with simple stellar population (SSP) models (based on PARSEC isochrones; Bressan et al. 2012). Our spectroscopic metallicity

**Table 5.** Literature metallicity determinations.

Object	[Fe/H]	Method	Ref.
NGC 147 HII	-1.2	a	SD2009
	$-1.7 \pm 0.4$	c	V2013
NGC 147 HIII	$-2.1 \pm 0.3$	c	V2013
	$-2.5 \pm 0.25$	b	DM88
NGC 147 SD7	-1.3	a	SD2009
	$-1.8 \pm 0.3$	c	V2013
NGC 147 PA-1	$-2.0 \pm 0.3$	c	V2013
NGC 147 PA-2	$-1.9 \pm 0.3$	c	V2013
NGC 6822 SC6	$-1.40^{+0.07}_{-0.04}$	d	V2015
	$-1.7 \pm 0.3$	c	V2015
NGC 6822 SC7	$-0.61^{+0.03}_{-0.04}$	d	V2015
	$-1.0 \pm 0.4$	c	V2015
M33 H38	$-1.10 \pm 0.10$	e	S98
M33 M9	$-1.64 \pm 0.28$	e	S98
M33 R12	$-1.19 \pm 0.24$	e	S98
	$-0.73 \pm 0.01$	a	S2010
M33 U49	$-1.64 \pm 0.20$	e	S98
	$-1.70 \pm 0.53$	b	BH91

**Notes.** (a): Spectral fitting; (b): Spectroscopic line indices; (c): Integrated broad-band colours (via relation from Kissler-Patig et al. 2002); (d): Integrated broad-band colours (via comparison with SSP models based on Bressan et al. 2012); (e): Red giant branch slope

**References.** DM88: Da Costa & Mould (1988); BH91: Brodie & Huchra (1991); SD2009: Sharina & Davoust (2009); V2013: Veljanoski et al. (2013); V2015: Veljanoski et al. (2015); S98: Sarajedini et al. (1998); S2010: Sharina et al. (2010)

determinations agree better with those based on the empirical colour-metallicity relation, whereas the metallicities based on SSP model comparisons appear to overestimated.

For the M33 clusters, our overlap with previous studies is limited. For U49, our metallicity determination agrees with the previous spectroscopic metallicity estimate by Brodie & Huchra (1991) within the (large) uncertainty on their measurement. For R12, our new metallicity is 0.22 dex lower than the spectroscopic estimate of  $[\text{Fe}/\text{H}] = -0.73 \pm 0.01$  of Sharina et al. (2010), although the 0.01 dex uncertainty on that measurement appears somewhat optimistic (the same paper quotes an overall metallicity of  $[\text{Z}/\text{H}] = -0.6 \pm 0.2$ ). Our measurements generally agree with those based on the RGB slope from Sarajedini et al. (1998), within the 0.1–0.3 dex uncertainties on those estimates.

#### 4.2. Metallicity distributions of globular clusters and field stars in NGC 147

It is well-known that the metallicity distributions of field stars and GCs in galaxies often differ substantially, with GCs being preferentially associated with the more metal-poor stellar populations (Forte et al. 1981; Forbes & Forte 2001; Harris & Harris 2002; Harris et al. 2007). This phenomenon is particularly extreme in some dwarf galaxies such as Fornax and WLM (L12, L14), where the GCs account for a significant fraction ( $\sim 1/5$ – $1/4$ ) of the metal-poor stars.

Our new metallicity determinations for GCs in NGC 147 allow us to carry out a similar comparison for this galaxy. The metallicity distribution for field stars in NGC 147 has been determined by Ho et al. (2014) via measurements of the Ca II infrared triplet. In Fig. 4 we plot a histogram of their metallicity measurements together with vertical bars indicating the GC metallicities.

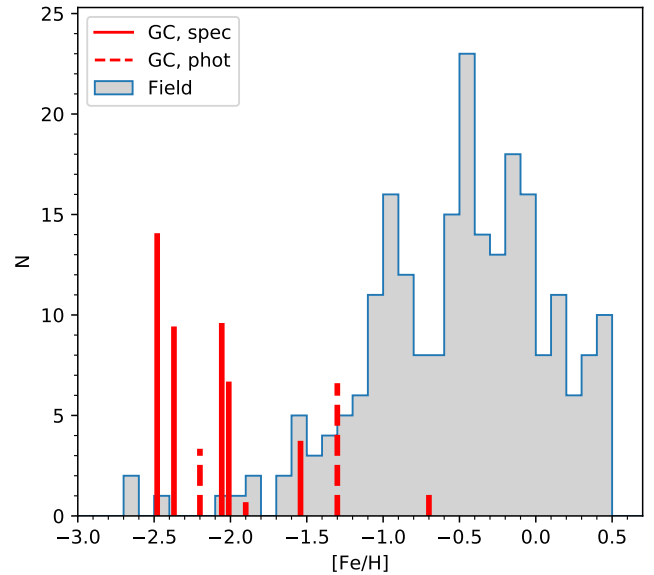


**Fig. 4.** Metallicity distributions of field stars (Ho et al. 2014) and GCs in NGC 147. For the GCs, the bars have been scaled according to the V-band luminosity of each cluster. Solid bars: this work. Dashed bars: Veljanoski et al. (2013).

The solid bars indicate our spectroscopic measurements whereas the dashed bars are the estimates by Veljanoski et al. (2013), which are based on broad-band colours. The lengths of the bars are scaled according to the luminosities of the GCs. Although we do not have spectroscopic measurements for all clusters, those for which we do have such measurements tend to be the brighter ones, which account for most of the mass and luminosity of the GC system.

The usual difference between GC and field star metallicity distributions is evident from Fig. 4. Ho et al. (2014) quote an average metallicity of  $\langle [\text{Fe}/\text{H}] \rangle = -0.51$  for the field stars, whereas most of the GCs have metallicities 1–2 dex below this value. In fact, there are so few metal-poor field stars that it is difficult to reliably estimate what fraction of the low-metallicity stars belong to GCs. Only five stars (out of a total of 230) have  $[\text{Fe}/\text{H}] < -2$ , corresponding to about 2.2% of the measured stars.

The outer regions of NGC 147 are perturbed due to tidal interactions with M31, which makes it challenging to estimate the total luminosity. McConnachie (2012) lists an absolute magnitude of  $M_V = -14.6$ , whereas Harris et al. (2013) give a value of  $M_V = -15.46 \pm 0.3$ . From a Sérsic profile fit, Crnojević et al. (2014) found  $M_V = -16.5$ . If we simply scale the luminosity estimated by Crnojević et al. (2014) by 2.2%, we then find that the metal-poor stars have a total magnitude of  $M_V = -12.34$ . The total luminosity of the GCs with  $[\text{Fe}/\text{H}] < -2.0$  corresponds to  $M_V = -9.42$ , or about 6.4% of the luminosity of the metal-poor stars. This is a lower fraction than those previously found for the Fornax dSph and WLM, but still substantially higher than for the Milky Way halo where the fraction is about 2% (e.g. L14). If we instead adopt the absolute magnitude from McConnachie (2012) then the fraction increases to 25%.

A more detailed calculation should account for the fact that translating the number fraction of bright metal-poor RGB stars to a total mass- or luminosity fraction requires knowledge of the star formation history. However, using isochrones from Dotter et al. (2007), we find that for a magnitude cut of  $M_I = -3$  (roughly corresponding to the magnitude limit in Ho et al.) the



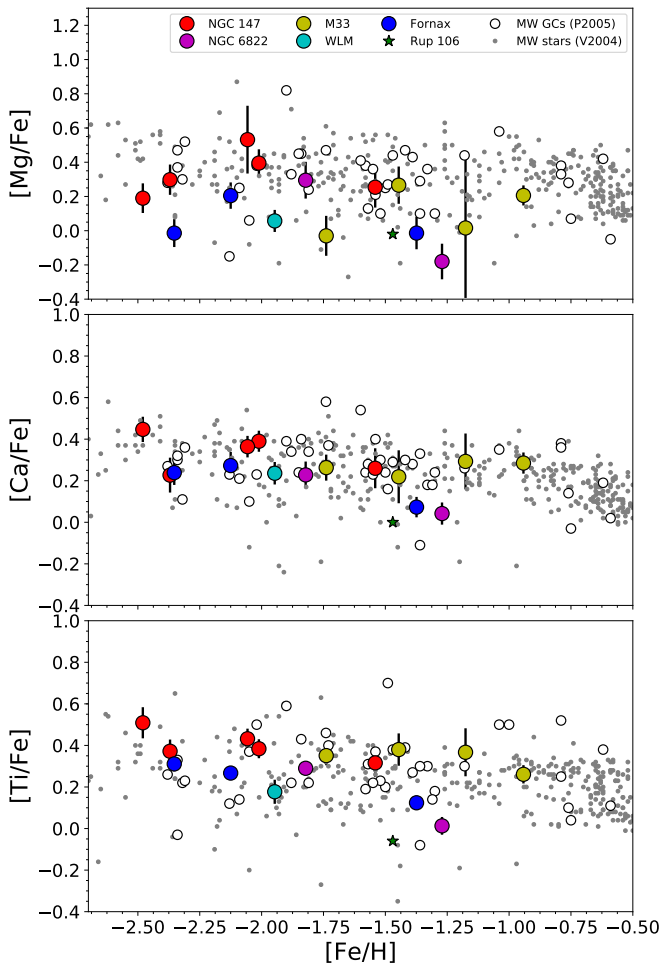


**Fig. 5.** Alpha-element abundances versus metallicity. Symbols are colour-coded according to host galaxy as indicated in the legend. Also included are data for Milky Way globular clusters (open circles, Pritzl et al. 2005) and field stars (grey dots, Venn et al. 2004). Data for the Galactic GC Rup 106 are shown with a green star (Villanova et al. 2013).

number of RGB stars per unit total luminosity is about independent of metallicity and age for ages  $> 4$  Gyr. From deep HST photometry, Geha et al. (2015) found that NGC 147 has an extended star formation history with a significant intermediate-age (5–7 Gyr) population. Hence, the number fraction of metal-poor stars may be used as a reasonable proxy for the contribution of metal-poor stars to the total luminosity of NGC 147. Ho et al. (2014) argue that biases in their spectroscopic metallicity distribution due to colour biases are likely small. Their spectra cover the full radial extent of NGC 147 and there are, in any case, no obvious gradients in the metallicity distribution (Crnojević et al. 2014). Clearly, a dominant uncertainty in the analysis carried out here is the small number of metal-poor stars.

### 4.3. Individual abundances

#### 4.3.1. Alpha-elements: Mg, Ca, Ti

In Fig. 5 we plot our measurements of the  $\alpha$ -element abundances ( $[Mg/Fe]$ ,  $[Ca/Fe]$ , and  $[Ti/Fe]$ ) as a function of  $[Fe/H]$ . For comparison we also include compilations of data for Milky Way

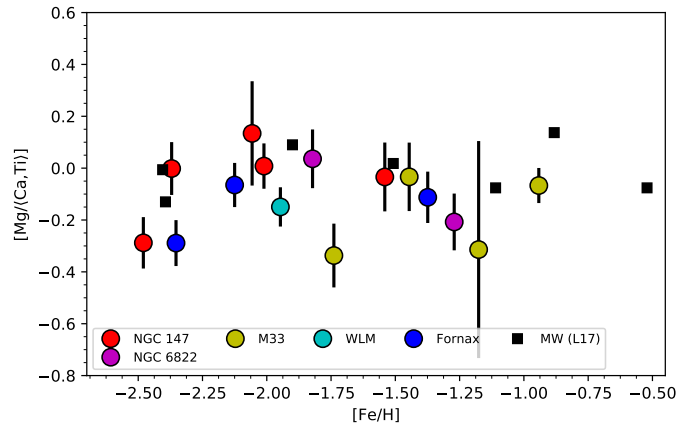


**Fig. 6.**  $[Mg/\langle Ca, Ti \rangle]$  for our integrated-light measurements. Also included are our data for Milky Way GCs (L17).

GCs (Pritzl et al. 2005) and field stars (Venn et al. 2004). At low metallicities ( $[Fe/H] \lesssim -1.5$ ), our integrated-light  $[Ca/Fe]$  and  $[Ti/Fe]$  ratios for extragalactic GCs are similar to those observed in Milky Way GCs and field stars, being enhanced relative to Solar-scaled abundance patterns by about 0.3 dex (i.e., about a factor of two). At higher metallicities we see a hint of a dichotomy between the abundance patterns in the M33 GCs and those in the dwarf galaxies (Fornax 4 and NGC 6822 SC7): the metal-rich M33 GCs remain  $\alpha$ -enhanced at about the same level as their more metal-poor counterparts, whereas the GCs in the dwarfs have lower  $[Ca/Fe]$  and  $[Ti/Fe]$  ratios. A lower degree of  $\alpha$ -enhancement in the more metal-rich GCs in the dwarfs is in accordance with the trend observed among field stars in nearby dwarf galaxies (Fornax, Sculptor, Sagittarius, Carina), in which  $[\alpha/Fe]$  decreases towards solar-scaled values between  $[Fe/H] = -2$  and  $[Fe/H] = -1$  (Tolstoy et al. 2009; Letarte et al. 2010; Hendricks et al. 2016). The GC Fornax 4 is thus consistent with the trends seen in the Fornax field stars, and our measurements for NGC 6822 SC7 provide the first evidence that a similar pattern exists for old stellar populations in NGC 6822.

In field stars,  $[Mg/Fe]$  tends to follow the same abundance patterns as other  $\alpha$ -elements, at least within the metallicity range probed here (McWilliam 1997; Tolstoy et al. 2009). Departures from this behaviour have previously been noted for integrated-light analyses of extragalactic GCs in M31 (Colucci et al. 2009, 2014), with  $[Mg/Fe]$  being lower than other  $\alpha$ -element ratios. Similar offsets have been seen in our own work (L12, L14). Such offsets might potentially be caused by internal Mg abundance spreads in the clusters, although Mg spreads that would be large enough to cause the observed effects are rare in Galactic GCs (Carretta et al. 2009). While our use of updated Mg oscillator strengths tends to reduce the difference, we see from Fig. 5 that there may still be a Mg deficiency for some clusters. To better assess the difference between Mg and the other  $\alpha$ -elements, we plot the ratio  $[Mg/\langle Ca, Ti \rangle]$  for our integrated-light measurements in Fig. 6. For comparison we also include our integrated-light measurements for seven Galactic GCs (Table B.2 in L17). Of the 15 extragalactic GCs, three (Hodge III, M33-M9, and Fornax 3) have relatively low ( $< -0.2$ )  $[Mg/\langle Ca, Ti \rangle]$  ratios, two more may also be depleted, although the difference with respect to the Milky Way sample is less significant given the errors (NGC 6822-SC7 and M33-H38), whereas the remaining clusters do not differ significantly from the Milky Way clusters.

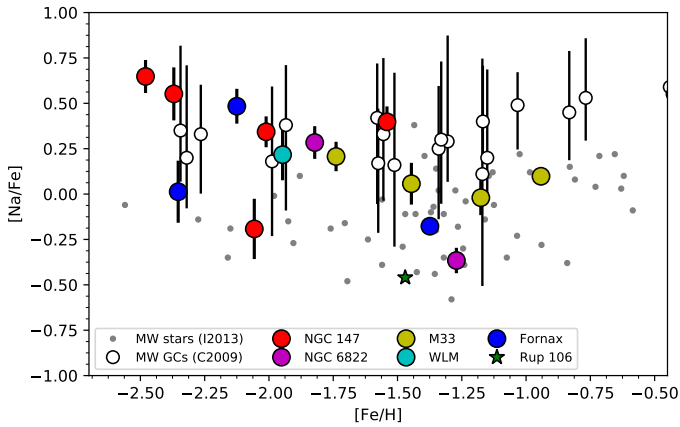


**Fig. 7.** Sodium abundances versus metallicity. Also included are data for Milky Way globular clusters (Carretta et al. 2009) and field stars (grey dots, Ishigaki et al. 2013).

It is worth asking how robust the apparently sub-solar  $[\text{Mg}/(\text{Ca}, \text{Ti})]$  ratios are. We first note that all clusters in Fig. 6 have been analysed using the same methodology, so that systematic effects and biases should be as minimal as possible. A closer look at the individual  $[\text{Mg}/\text{Fe}]$  measurements for Hodge III, M33-M9, and Fornax 3 (Tables A.2, A.9, and A.13) shows that the low average Mg abundances are not driven by a single outlying measurement. For Hodge III, all four individual measurements give  $[\text{Mg}/\text{Fe}]$  ratios below the average  $[\text{Ca}/\text{Fe}]$  and  $[\text{Ti}/\text{Fe}]$  ratios, and the weighted rms ( $\text{rms}_w = 0.15$  dex) is comparable to the individual errors (0.10–0.21 dex), which suggests that most of the line-to-line scatter can be accounted for by the random measurement uncertainties. For M33-M9,  $\text{rms}_w$  is again similar to the errors on the individual measurements, all of which indicate low  $[\text{Mg}/\text{Fe}]$  values, although in this case only three lines could be measured. For Fornax 3, the weighted rms is somewhat larger than the individual errors. The Mg I line at 5711 Å gives  $[\text{Mg}/\text{Fe}] = +0.34 \pm 0.11$ , which is consistent with the average  $[\text{Ca}/\text{Fe}]$  and  $[\text{Ti}/\text{Fe}]$  ratios, but the other four Mg lines all yield  $[\text{Mg}/\text{Fe}] < +0.1$ . For M33-H38, the uncertainty on the  $[\text{Mg}/\text{Fe}]$  measurement (based on only two lines) is so large that no meaningful statement can be made, whereas the moderately low  $[\text{Mg}/(\text{Ca}, \text{Ti})]$  ratio for NGC 6822-SC7 is indeed, to some extent, driven by one line (Mg I at 4352 Å). In summary, we only consider the sub-solar  $[\text{Mg}/(\text{Ca}, \text{Ti})]$  ratios in the three GCs Hodge III, M33-M9, and Fornax 3 as relatively robust.

#### 4.3.2. Sodium

Figure 7 shows our integrated-light measurements of  $[\text{Na}/\text{Fe}]$ , together with data for Milky Way field stars (Ishigaki et al. 2013) and globular clusters (Carretta et al. 2009). For the Carretta et al. data, the vertical bars show the range of  $[\text{Na}/\text{Fe}]$  values observed within the clusters and the open circles indicate the average values. The lower end of the range of  $[\text{Na}/\text{Fe}]$  values typically coincides with the abundances observed in the field, while GCs contain stars in which the  $[\text{Na}/\text{Fe}]$  ratios are enhanced by up to about 0.5 dex. Consequently, the average  $[\text{Na}/\text{Fe}]$  ratios in GCs are higher compared to those seen in the field.

For most of the extragalactic GCs, the integrated-light  $[\text{Na}/\text{Fe}]$  ratios resemble the average values in Milky Way GCs in being elevated, but again there are a few exceptions. We find

relatively low  $[\text{Na}/\text{Fe}]$  ratios for NGC 147 SD7 and Fornax 3, although the Na lines are weak in these metal-poor clusters (cf. Fig. 2) and the uncertainties on the measurements are relatively large. We note that the 6154/6161 Å lines give a higher sodium abundance of  $[\text{Na}/\text{Fe}] = +0.43 \pm 0.19$  for NGC 147 SD7, while no abundance could be determined from these lines for Fornax 3. However, we remind the reader that the Na abundance for Fornax 3 might be affected by the bad pixels near the 5688 Å line. Potentially more significant are the low  $[\text{Na}/\text{Fe}]$  ratios of the two more metal-rich GCs, NGC 6822 SC7 and, to a lesser extent, Fornax 4. In both cases, the 6154/6161 Å lines confirm sub-solar  $[\text{Na}/\text{Fe}]$  ratios, albeit with a large uncertainty for NGC 6822 SC7. This may simply reflect the general tendency for Na to be relatively under-abundant in dwarf galaxies, with typical abundance ratios of  $[\text{Na}/\text{Fe}] \simeq -0.5$  at intermediate metallicities (Shetrone et al. 2003; Tolstoy et al. 2009). No information on the detailed abundances of halo field stars is available for NGC 6822. However, we recall that NGC 6822 SC7 also has relatively low  $\alpha$ -element abundance ratios, comparable to those of Fornax 4. Hence, our measurements of  $[\text{Na}/\text{Fe}]$  may still leave room for an enhanced mean Na abundance relative to the (unknown) “baseline” level in the field stars.

The M33 GCs may also have slightly lower  $[\text{Na}/\text{Fe}]$  ratios than Milky Way GCs at the same metallicity, but interpretation is again complicated by our lack of knowledge about the Na abundances in M33 halo field stars. Additionally, we note that the absolute scale of the Na abundances is somewhat uncertain, as our integrated-light measurements do not currently include corrections for non-LTE effects, which are often applied to measurements of individual stars. These corrections can reach 0.2–0.3 dex, but their magnitude (and even the sign) depends on the gravity, temperature, and composition of the star (Gratton et al. 1999). In L17 we found that our integrated-light  $[\text{Na}/\text{Fe}]$  ratios for Galactic GCs were systematically slightly lower (by 0.08–0.14 dex, depending on the comparison sample) than average values derived from analysis of individual stars, which suggests that our integrated-light Na abundances may be underestimated by approximately that amount.

#### 4.3.3. Iron-peak elements: Sc, Cr, Mn, Ni

In Fig. 8 we show the iron-peak element abundances (Sc, Cr, Mn, Ni). These elements are usually unaffected by the presence of multiple populations in GCs and thus display similar behaviour in GCs and field stars. Our integrated-light abundance ratios for these elements are fairly similar to those observed in the Milky Way. Manganese follows the well-known trend of increasing from  $[\text{Mn}/\text{Fe}] \simeq -0.5$  at low metallicities to  $[\text{Mn}/\text{Fe}] \simeq 0$  at higher metallicities (Nissen et al. 2000), although this trend may be mainly an artefact of non-LTE effects (Bergemann & Gehren 2008; Battistini & Bensby 2015). Perhaps significantly, the two most metal-poor clusters (both in NGC 147) have high  $[\text{Mn}/\text{Fe}]$  ratios.

NGC 6822 SC7 and Fornax 4 are, once again, outliers in some of these relations, with relatively low  $[\text{Sc}/\text{Fe}]$  and  $[\text{Ni}/\text{Fe}]$  ratios. In this sense, they resemble the Galactic globular cluster Ruprecht 106, which is marked with an asterisk (Villanova et al. 2013). The low Sc abundances in these clusters are consistent with the correlation between Sc and the  $\alpha$ -elements observed in Galactic field stars (Nissen et al. 2000; Ishigaki et al. 2013).

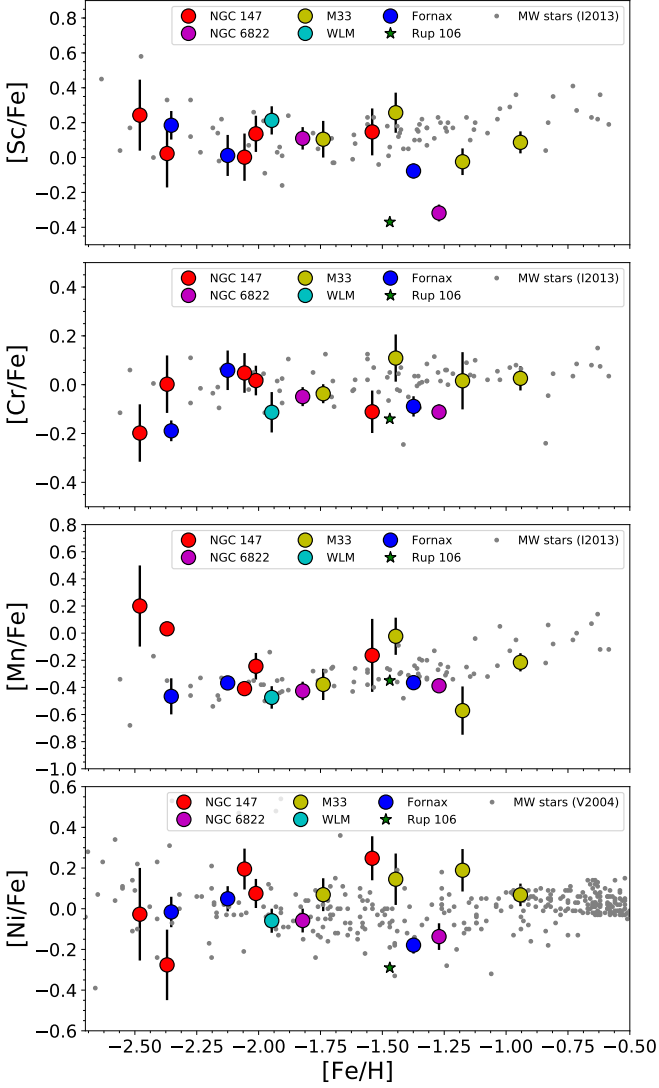


**Fig. 8.** Iron-peak element abundances versus metallicity. Also included are data for Milky Way field stars (grey dots, Ishigaki et al. 2013; Venn et al. 2004).

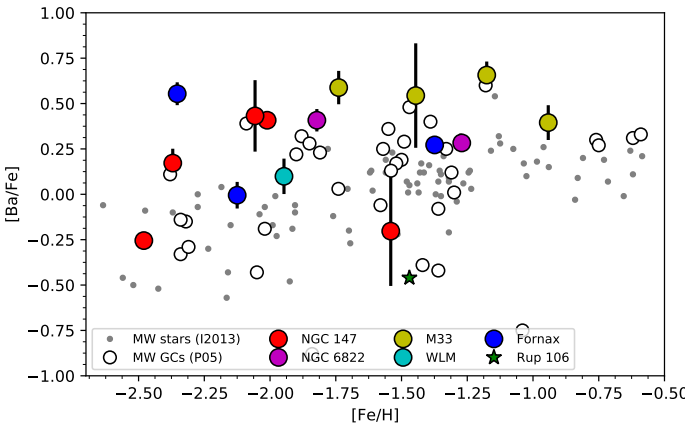


**Fig. 9.** Barium abundances versus metallicity. Also included are data for Milky Way globular clusters (Pritzl et al. 2005) and field stars (grey dots, Ishigaki et al. 2013).

#### 4.3.4. Barium

The  $[\text{Ba}/\text{Fe}]$  ratios show substantial scatter (Fig. 9), but the GCs in the dwarf galaxies (except Fornax 3) mostly have Ba abundances compatible with those in Galactic GCs. As discussed in L12, Letarte et al. (2006) found lower  $[\text{Ba}/\text{Fe}]$  ratios for three individual stars in Fornax 3 (between  $[\text{Ba}/\text{Fe}] = +0.09$  and  $+0.27$ ), and although the value found here is lower than that quoted in L12 (due to the modifications in our analysis discussed at the beginning of Sec. 4), an offset remains.

The GCs in M33 all have relatively high Ba abundances,  $[\text{Ba}/\text{Fe}] \approx +0.5$ , that are rare among Galactic GCs. It is worth noting that since the Ba lines are quite strong, especially at higher metallicities, they are also relatively sensitive to details of the atmospheres, hyperfine structure, NLTE effects, etc., which might introduce significant systematic uncertainties. In L17 we found that our integrated-light measurements may overestimate the  $[\text{Ba}/\text{Fe}]$  ratios by 0.20-0.35 dex at the lowest metallicities ( $[\text{Fe}/\text{H}] \lesssim -2$ ), compared to literature data for individual stars, although better agreement was found for more metal-rich clusters. From Fig. 9, the Milky Way GCs and field stars do show a trend of increasing  $[\text{Ba}/\text{Fe}]$  with metallicity, and if our measurements were shifted downwards by roughly 0.2 dex they would match the Milky Way data quite closely. Thus, the evidence for enhanced  $[\text{Ba}/\text{Fe}]$  in the M33 GCs should be considered somewhat tentative at this point.

## 5. Discussion

### 5.1. Metallicities

Our measurements confirm that GCs in dwarf galaxies tend to be relatively metal-poor, compared both with their counterparts in the Milky Way halo and with the field stars in the respective galaxies. In the Milky Way, 13 out of 152 GCs (slightly less than 9%) have metallicities  $[\text{Fe}/\text{H}] < -2$ . In Fornax, four out of five GCs fall in this range, and in NGC 147 this is true for four of the five bright GCs for which we have spectroscopic metallicities. In NGC 6822 we only have data for two GCs, but again both of these fall below the peak of the field star metallicity distribution at  $[\text{Fe}/\text{H}] = -0.84$  (Swan et al. 2016). Nevertheless, it may be notable that none of the GCs for which we have obtained accurate metallicity determinations until now have metallicities below  $[\text{Fe}/\text{H}] \approx -2.5$ .

The difference between the metallicity distributions of the field stars and GCs is striking: at metallicities above  $[\text{Fe}/\text{H}] = -2$ , Fornax has only one GC (Fornax 4), which accounts for about 0.4% of the luminosity of the field stars. In NGC 147 the fraction is still lower, 0.04%. These numbers may be compared with the corresponding fractions of  $\sim 20\%$  and  $\sim 6\%$  at the low-metallicity end. It is illustrative to compare these ratios with the specific GC frequencies and -luminosities in larger galaxies. Forbes et al. (2001) noted that the “bulge specific frequency” is about constant at  $S_N \approx 1$  for spirals and ellipticals. For an average GC luminosity of  $L_V \approx 10^5 L_{\odot,V}$ , this corresponds to a specific GC luminosity of about 0.1%. This number is not very different from those found for the metal-rich components of Fornax and NGC 147, especially when the poor statistics are taken into account.

Lamers et al. (2017) proposed that differences in GC specific luminosity are caused primarily by more efficient destruction of metal-rich clusters in their gas-rich natal environments. However, they also noted that more continuous, low-level star formation may disfavour the formation of massive clusters. In



many present-day star forming environments, the mass function of young clusters can be approximated by a Schechter-like function  $dN/dM \propto M^{-2} \exp(-M/M_c)$  (Larsen 2009) where the truncation mass  $M_c$  scales with the star formation rate surface density,  $\Sigma_{\text{SFR}}$  (Johnson et al. 2017). Hence, a low  $\Sigma_{\text{SFR}}$  might account for a lack of massive cluster formation.

The star formation history of the Fornax dwarf has been studied in detail by de Boer et al. (2012), who found a peak star formation rate of  $(3-4) \times 10^{-3} M_{\odot} \text{ yr}^{-1}$  between 5 and 10 Gyr ago. Combined with a half-number radius of 19' or 750 pc (Battaglia et al. 2006), this gives an average  $\Sigma_{\text{SFR}} \approx 1 \times 10^{-3} M_{\odot} \text{ yr}^{-1} \text{ kpc}^{-2}$  within the half-number radius. This is about an order of magnitude lower than the  $\Sigma_{\text{SFR}}$  values typical of normal disc galaxies in the Local Universe (Kennicutt 1998). From the relation in Johnson et al. (2017), this  $\Sigma_{\text{SFR}}$  would correspond to a truncation mass of  $M_c \approx 4000 M_{\odot}$ , which would naturally explain why Fornax did not form any massive clusters for most of its lifetime.

In NGC 147, about half of the stars appear to have formed during the peak of star formation between 5–7 Gyr ago (Geha et al. 2015). Assuming  $M_V = -16.5$ , NGC 147 is about 3.3 mag brighter than Fornax, and if we scale the stellar mass of Fornax (Coleman & de Jong 2008) accordingly (ignoring differences in the detailed star formation histories), then the total stellar mass of NGC 147 is  $M \sim 1.3 \times 10^9 M_{\odot}$ , which translates to a peak SFR of  $\sim 0.32 M_{\odot} \text{ yr}^{-1}$ . For a half-light radius of 1.4 kpc (Crnojević et al. 2014), we then get  $\Sigma_{\text{SFR}} = 0.025 M_{\odot} \text{ yr}^{-1} \text{ kpc}^{-2}$  within the half-light radius, which is more than an order of magnitude higher than for Fornax. Using the relation in Johnson et al. (2017), this gives a truncation mass of  $M_c = 1.3 \times 10^5 M_{\odot}$ , suggesting that some relatively massive clusters might have formed in NGC 147 during this epoch. Given that there are few, if any, GCs associated with the metal-rich field stars in NGC 147, cluster disruption may indeed have played a more important role in NGC 147.

The more important question may be why dwarf galaxies were so proficient at forming metal-poor GCs that managed to survive until today, rather than why they did not form any metal-rich ones. Here, it is worth noting that the relatively crude age resolution even in the detailed CMD-based study by de Boer et al. (2012) makes it difficult to distinguish between smooth SFHs and more bursty ones. Hence, the metal-poor GCs could have formed during brief, intense bursts of star formation early in the evolutionary histories of the galaxies.

One possible way to distinguish between low formation efficiencies and high disruption efficiencies would be to look for stars with GC-like abundance patterns among metal-rich field stars. If such stars exist, it would favour a picture in which massive GCs did form, but were subsequently destroyed. So far, no significant populations of field stars with GC-like abundance patterns have been found in dwarf galaxies (Lemasle et al. 2014; Lardo et al. 2016; Suda et al. 2017), but the samples may still be too small to rule out an enriched fraction of a few percent, similar to that seen in the Milky Way halo (Martell et al. 2011, 2016).

## 5.2. Detailed abundances

### 5.2.1. Overall trends and chemical enrichment histories

In terms of their detailed abundance patterns, the metal-poor GCs in the dwarf galaxies studied here are similar to metal-poor GCs in the Milky Way halo. The  $\alpha$ -elements (Ca, Ti) are enhanced by  $\sim 0.3$  dex relative to Solar-scaled abundance patterns. While usually classified as an iron-peak element, Sc also tends to

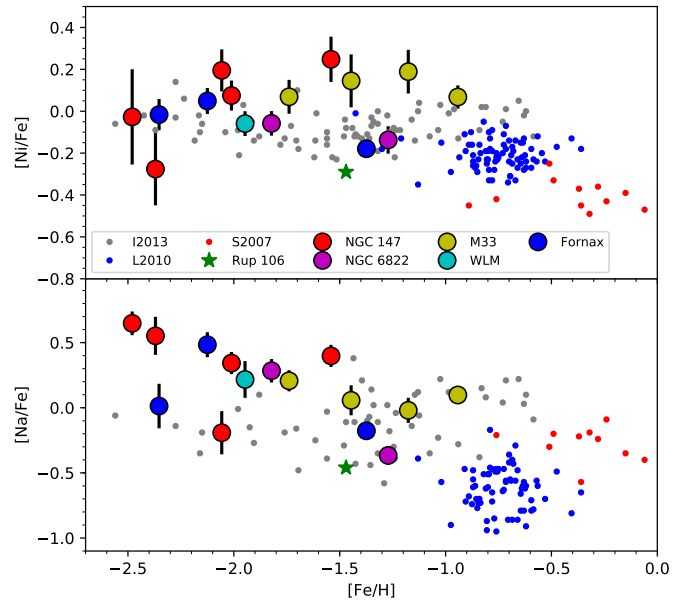


**Fig. 10.** [Ni/Fe] and [Na/Fe] with data for stars in the Fornax dSph (blue dots, Letarte et al. 2010) and in Sagittarius (red dots, Sbordone et al. 2007) also included.

be enhanced in metal-poor,  $\alpha$ -enhanced populations in the Milky Way (Nissen et al. 2000; Fishlock et al. 2017). In our observations, we see the same pattern of slightly super-solar [Sc/Fe] ratios in the metal-poor,  $\alpha$ -enhanced GCs. This suggests that, at least to first order, the early chemical enrichment histories were quite similar in these different environments.

More significant differences compared to Milky Way GCs start to become apparent for the more metal-rich clusters, Fornax 4 and NGC 6822 SC7. We have already noted the general similarity of the abundance patterns in these clusters to those observed in field stars in nearby dwarf galaxies. Thus, it appears that GCs are indeed useful tracers of the chemical evolutionary histories in their parent galaxies. The important caveat here, of course, is the difference in the metallicity distributions of field stars and GCs, which means that it is not straight-forward to make general statements about *distributions* of abundances and abundance ratios from GCs. However, GCs can provide useful information on *trends*, such as  $[\alpha/\text{Fe}]$  vs.  $[\text{Fe}/\text{H}]$  and correlations between these quantities and *age* (to the extent that ages of the GCs are known).

### 5.2.2. Evidence for multiple populations: Mg spreads and the Na-Ni relation

In most clusters, Mg follows the same abundance patterns as the other  $\alpha$ -elements. In the few (3–5) cases where significant deviations occur, they are in the sense that Mg is depleted relative to Ca and Ti. This may suggest the presence of Mg abundance anomalies within the affected clusters, although significantly depleted [Mg/Fe] ratios would require much more extreme Mg anomalies than those observed in most Milky Way GCs. In M15, which has a relatively extended Mg-Al anticorrelation (Snedden et al. 1997), the integrated-light [Mg/Fe] ratio is only slightly depleted with respect to Ca and Ti, with  $[\text{Mg}/(\text{Ca}, \text{Ti})] = -0.13$  according to our integrated-light measurements (L17; see also

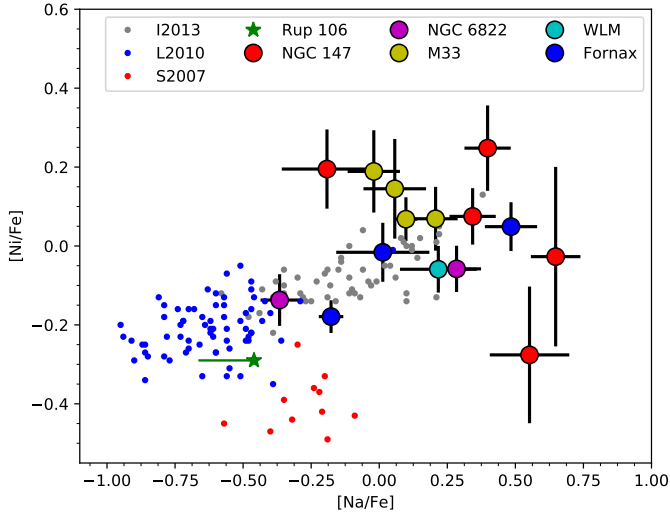


**Fig. 11.**  $[\text{Ni}/\text{Fe}]$  vs.  $[\text{Na}/\text{Fe}]$ . Also included: stars in the Milky Way (grey dots, Ishigaki et al. 2013), in the Fornax dSph (blue dots, Letarte et al. 2010), and in Sagittarius (red dots, Sbordone et al. 2007).

Fig. 6). To produce a depletion of more than 0.2 dex in the average  $[\text{Mg}/\text{Fe}]$ , more extreme Mg anomalies would be required, such as those seen in the Galactic GC NGC 2419 for which  $[\text{Mg}/\text{Fe}]$  ratios as low as  $-1$  dex are observed (Mucciarelli et al. 2012; Cohen et al. 2011; Cohen & Kirby 2012). For this cluster, Mucciarelli et al. (2012) found  $\langle [\text{Mg}/\text{Fe}] \rangle = +0.05 \pm 0.08$ ,  $\langle [\text{Ca}/\text{Fe}] \rangle = +0.46 \pm 0.01$ , and  $\langle [\text{Ti}/\text{Fe}] \rangle = +0.29 \pm 0.02$ , indicating a Mg depletion of 0.41 and 0.24 dex relative to Ca and Ti, respectively, which is comparable to the depletion seen in the extragalactic GCs.

The clusters in our sample that have depleted  $[\text{Mg}/\langle \text{Ca}, \text{Ti} \rangle]$  ratios do not appear to have particularly unusual abundances of Na or other elements. Within the Milky Way GC population, some clusters with substantial Mg spreads do display anti-correlated  $[\text{Na}/\text{Fe}]$  and  $[\text{Mg}/\text{Fe}]$  abundances (e.g. M15; Sneden et al. 1997), while others do not (e.g. NGC 2419; Cohen & Kirby 2012). Furthermore, while Na spreads are nearly ubiquitous, significant Mg spreads are not (Carretta et al. 2009). Perhaps, with larger samples, patterns will emerge, but at this point the origin of large Mg spreads and their exact relation to other abundance ratios remain unclear.

More generally, the  $[\text{Na}/\text{Fe}]$  ratios represent a potentially promising diagnostic for identifying multiple populations in extragalactic GCs. The spread in  $[\text{Na}/\text{Fe}]$  is substantial in most Galactic GCs ( $\sim 0.5$  dex; Carretta et al. 2009), and the  $[\text{Na}/\text{Fe}]$  ratios observed in integrated light observations are elevated well above the level seen in field stars (L17; Sakari et al. 2013; Colucci et al. 2017). Our measurements here show a similar enhancement in most of the metal-poor GCs, whereas the more metal-rich clusters tend to have lower  $[\text{Na}/\text{Fe}]$  ratios. A better understanding of possible systematics in the Na abundance measurements, such as non-LTE effects, would be desirable to quantify the significance of such trends. A complication here is that the field star Na abundances are not necessarily the same in the extragalactic environments as in the Milky Way halo (Sect. 4.3; Shetrone et al. 2003; Cohen & Huang 2009, 2010; Letarte et al. 2010; Lemasle et al. 2014; Hendricks et al. 2016).

For extragalactic applications, it may not always be feasible to obtain detailed abundance measurements for individual field

**Table 6.** Differences between abundances based on the most recent Kurucz line list and those in Table 4.

	$\langle \Delta_{\text{Kur}-\text{CH04}} \rangle$	$\sigma$
$[\text{Fe}/\text{H}]$	$-0.016$	$0.014$
$[\text{Na}/\text{Fe}]$	$+0.017$	$0.014$
$[\text{Mg}/\text{Fe}]$	$+0.048$	$0.025$
$[\text{Ca}/\text{Fe}]$	$+0.023$	$0.016$
$[\text{Sc}/\text{Fe}]$	$+0.099$	$0.049$
$[\text{Ti}/\text{Fe}]$	$-0.017$	$0.036$
$[\text{Cr}/\text{Fe}]$	$+0.035$	$0.037$
$[\text{Mn}/\text{Fe}]$	$+0.069$	$0.057$
$[\text{Ni}/\text{Fe}]$	$-0.054$	$0.157$
$[\text{Ba}/\text{Fe}]$	$-0.055$	$0.074$

stars, and it would therefore be desirable with other methods to establish the reference Na abundances against which data for GCs could be compared. In this regard, the  $[\text{Ni}/\text{Fe}]$  ratio may be a useful option, as it is correlated with  $[\text{Na}/\text{Fe}]$  in Galactic field stars (Nissen & Schuster 1997, 2010). The correlation has also been extended to dwarf galaxies (Tolstoy et al. 2009; Cohen & Huang 2009, 2010; Lemasle et al. 2014). The origin of the Na-Ni correlation in field stars is suggested to be linked to explosive nucleosynthesis in type II SNe (Letarte et al. 2010), so it should be independent of the hydrogen-burning processes that are usually invoked to explain abundance anomalies in GCs (e.g. Gratton et al. 2012). However, since Ni is also produced in large amounts in type Ia SNe, the exact behaviour of the Na-Ni correlation is expected to depend on the detailed chemical enrichment history, and may well differ from one galaxy to another.

Fig. 10 shows our measurements of  $[\text{Na}/\text{Fe}]$  and  $[\text{Ni}/\text{Fe}]$  vs.  $[\text{Fe}/\text{H}]$ , now together with data for field stars in the Fornax dwarf (Letarte et al. 2010) and Sagittarius (Sbordone et al. 2007), and in Fig. 11 we plot the same data in the  $[\text{Na}/\text{Fe}]$  vs.  $[\text{Ni}/\text{Fe}]$  plane. At this stage, it is not clear that unambiguous conclusions about Na enrichment in the GCs can be drawn directly from Fig. 11. Clusters with additional Na enrichment (beyond that following from the Na-Ni correlation) should lie to the right of the sequence formed by the field stars, but there is no clear tendency in Fig. 11 for this to actually be the case. Instead, there is a large scatter around the locus occupied by the stars. Some of this scatter may well be due to observational uncertainties - in particular, for the two most metal-poor GCs in NGC 147 (N147-PA-1 and Hodge III), most of the individual measurements of  $[\text{Ni}/\text{Fe}]$  are upper limits or did not converge, and the remaining 4–5 measurements for each of these clusters show a large dispersion. We have noted (Sec. 4.3.2) that the Na abundances may be underestimated by  $\sim 0.1$  dex, and an increase of the  $[\text{Na}/\text{Fe}]$  ratios by this amount would indeed shift the data points in Fig. 11 to the right. Alternatively, it is also possible that the  $[\text{Ni}/\text{Fe}]$  ratios are systematically overestimated, and we note that the line-to-line scatter on the Ni abundances in Table 4 is indeed quite large for most clusters.

A complicating factor in this comparison is that the different galaxies occupy distinct loci in Fig. 11, with the Sbordone et al. (2007) measurements for Sagittarius being offset from the others. While this might be due to different enrichment histories, we note that Hasselquist et al. (2017) find Ni and Na abundance ratios for Sagittarius closer to those seen in Fornax. They find a mean  $[\text{Na}/\text{Fe}] \simeq -0.6$  (with a large scatter) and  $[\text{Ni}/\text{Fe}] \simeq -0.2$  for  $-0.8 < [\text{Fe}/\text{H}] < 0$ , which would largely remove the offset between the Fornax and Sagittarius measurements. Another problem in making these comparisons is that the field stars in



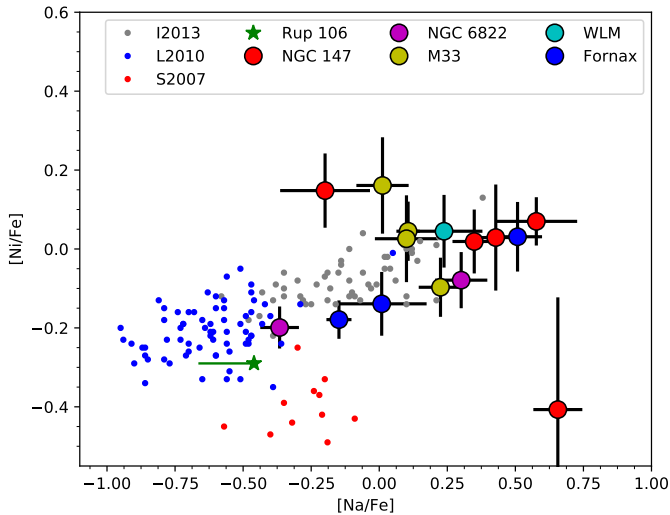


**Fig. 12.** Same as Fig. 11, but using the most recent line list from the Kurucz web site.

Fornax and Sagittarius, for which Na and Ni abundances are available, generally have higher metallicities than the GCs in our sample (Fig. 10), so it is unclear whether the more metal-poor stars in the dwarf galaxies follow the same  $[\text{Ni}/\text{Fe}]$  vs.  $[\text{Na}/\text{Fe}]$  relation as stars in the Milky Way.

### 5.2.3. Analysis with Kurucz line list

An important source of systematic uncertainty is the input line list used in the analysis. As recently pointed out by Laverick et al. (2017), the atomic data included in different databases can differ substantially. Differences in the input line list can affect our abundances not only through the data for the measured individual lines themselves, but also via other nearby lines that may be blended with a particular feature of interest or affect the scaling of the spectra when carrying out the fits.

In L17 we compared results based on our “standard” line list with fits based on a more recent version of the Kurucz list. The Kurucz list is updated regularly and here we have carried out an additional set of fits to the GC spectra in the current sample using the most recent version (dated 08-Oct-2017). The results of these fits are given in the Appendix (Table B.1) and Table 6 lists the mean differences between the abundances in Table 4 and those in Table B.1, as well as the cluster-to-cluster dispersions. As found in L17, the differences are fairly small, in all cases less than 0.1 dex, and the conclusions based on our modified version of the CH04 line list remain mostly unchanged. The  $[\text{Na}/\text{Fe}]$  ratios increase very slightly, by 0.017 dex (mostly driven by a corresponding decrease in  $[\text{Fe}/\text{H}]$ ), and the average  $[\text{Mg}/\text{Fe}]$  ratios increase by about 0.05 dex, but the three Mg-depleted clusters remain so also when using the new Kurucz line list. The  $[\text{Ba}/\text{Fe}]$  ratios decrease by about 0.05 dex, but this is not enough to remove the offset in Fig. 9. Fornax 4 and NGC 6822-SC7 remain less  $\alpha$ -enhanced than their counterparts at similar metallicities in M33 and the Milky Way.

The scatter in Table 6 is again particularly large for  $[\text{Ni}/\text{Fe}]$ , and it is thus worth examining how this may affect Fig. 11. In Fig. 12 we show the  $[\text{Ni}/\text{Fe}]$  vs.  $[\text{Na}/\text{Fe}]$  plot once again, but using the measurements based on the Kurucz line list. There is now a somewhat clearer tendency for the GC measurements to

fall to the right of, or below, the relation followed by the stars, although a substantial scatter remains and there are still a couple of clusters on the “wrong” side of the relation. Note that we still haven’t accounted for possible systematic errors on  $[\text{Na}/\text{Fe}]$ , which might shift the data points further towards the right.

### 5.2.4. NGC 6822 SC7: A “twin” of Ruprecht 106

Finally, we comment on the remarkable similarity of the abundance patterns of NGC 6822 SC7 to those in the peculiar Galactic GC Ruprecht 106, for which we have indicated the abundance measurements by Villanova et al. (2013) with green asterisks in Fig. 5 and Figs. 7-9. Like NGC 6822 SC7, Ruprecht 106 shows no enhancement of the  $\alpha$ -elements, and Na, Sc, and Ni are all significantly depleted compared to more typical Milky Way GC abundance patterns. The one dissimilarity is for Ba, which is depleted in Ruprecht 106 but about normal in NGC 6822 SC7. The suggestion that the unusual abundance patterns in Ruprecht 106 indicate an extragalactic origin (Villanova et al. 2013) may be supported by the similarity to NGC 6822 SC7.

A noteworthy property of Ruprecht 106 is that it appears to be chemically *homogeneous*, i.e., it shows no evidence for multiple stellar populations. The similarity of the abundance patterns, in particular Na and Ni, might suggest that this is true also for NGC 6822 SC7. Again, Fig. 11 does not offer a clear-cut conclusion: in fact, Ruprecht 106 is offset with respect to the mean  $[\text{Ni}/\text{Fe}]$  vs.  $[\text{Na}/\text{Fe}]$  relation for field stars in Fornax in the direction that would suggest Na-enrichment. (We have used the LTE Na abundance from Villanova et al. (2013) for comparison with our measurements; using their NLTE abundance would shift the point as indicated by the green line, closer to the field stars.) However, if anything the evidence against multiple populations would then appear *stronger* in NGC 6822 SC7, which falls closer to the locus of the field stars. Villanova et al. (2013) suggested that the apparent absence of multiple populations in Rup 106 might be related to its relatively low mass. For NGC 6822 SC7, such an explanation cannot be invoked. The velocity dispersion is the highest among the clusters studied here, and the absolute magnitude is  $M_V = -8.6$ , corresponding to a mass of  $\sim 3.5 \times 10^5 M_\odot$  (assuming a mass-to-light ratio of  $\sim 1.5$ ). However, we emphasise that the current evidence does not allow us to establish with certainty that multiple populations are absent from SC7.

## 6. Summary

We have presented new integrated-light measurements of chemical abundances for 11 globular clusters in NGC 147, NGC 6822, and Messier 33. Combined with our previous data for GCs in the Fornax and WLM galaxies, we have now carried out such measurements for 15 Local Group GCs. Our principal findings are as follows:

- The GCs in the dwarf galaxies tend to be more metal-poor on average than GCs in the Galactic halo. Nevertheless, it may be significant that no GCs with  $[\text{Fe}/\text{H}] \lesssim -2.5$  have yet been found, neither in the Milky Way nor among the clusters we have observed so far.
- The  $[\alpha/\text{Fe}]$  ratios behave differently as a function of metallicity in the dwarf galaxies and M33: While all metal-poor clusters ( $[\text{Fe}/\text{H}] \lesssim -1.5$ ) are  $\alpha$ -enhanced at about the same level as Milky Way GCs, the more metal-rich GCs in the dwarf galaxies have close to Solar  $[\alpha/\text{Fe}]$  ratios, while those in M33 remain  $\alpha$ -enhanced.

- In most clusters, Mg follows the other  $\alpha$ -elements, Ca and Ti. A small subset of the clusters have depleted [Mg/Fe] ratios (by 0.2–0.3 dex) relative to Ca and Ti, as found previously in other extragalactic GCs.
- In the metal-poor GCs, [Na/Fe] is elevated as in Milky Way GCs, consistent with the presence of Na-rich stars in the clusters. In the more metal-rich clusters, the [Na/Fe] ratios are generally lower than in Milky Way GCs, in particular in Fornax 4 and the cluster SC7 in NGC 6822. However, since we lack information about Na abundances at the same metallicities in the field stars, the implications for the presence of multiple populations are unclear.
- Fornax 4 and SC7 also have low [Ni/Fe] ratios, as observed also in field stars in nearby dwarf galaxies.
- The [Ba/Fe] ratios show a large spread, but may be systematically elevated in the M33 GCs. Interpretation of such an offset is complicated by the fact that Ba can be produced by both the  $r$ - and  $s$ -process. Constraining the relative importance of the  $r$ - and  $s$ -process requires information about other  $n$ -capture elements, such as Eu. This, however, requires better sensitivity in the blue part of the spectrum than we have achieved here.

In the dwarf galaxies, the trends followed by the GCs are generally consistent with data for field stars in nearby dwarf galaxies, and our measurements provide the first evidence of the “knee” in the  $[\alpha/\text{Fe}]$  vs.  $[\text{Fe}/\text{H}]$  relation in NGC 6822. The measurements presented here also provide the first detailed information on chemical abundances in the M33 halo. The  $\alpha$ -elements in the M33 GCs follow patterns similar to those seen in Milky Way GCs, which suggests that the M33 halo underwent relatively rapid chemical enrichment, dominated by Type II SN nucleosynthesis. The tentative nature of the results regarding barium must be stressed, but we note that elevated [Ba/Fe] ratios would be reminiscent of those observed in some dwarf galaxies, possibly indicating a stronger contribution to chemical enrichment by AGB stars in M33 than in the Milky Way halo. The combination of Na and Ni abundance measurements may ultimately turn out to be useful for detecting multiple populations in integrated-light observations, provided that an accuracy of  $\sim 0.1$  dex or better can be reached for the integrated-light abundance measurements. However, this also requires a better understanding of the Na-Ni relation in extragalactic environments.

**Acknowledgements.** We thank the anonymous referee for a careful reading of the manuscript and a number of helpful comments. This research has made use of the NASA/IPAC Extragalactic Database (NED) which is operated by the Jet Propulsion Laboratory, California Institute of Technology, under contract with the National Aeronautics and Space Administration. This work has made use of the VALD database, operated at Uppsala University, the Institute of Astronomy RAS in Moscow, and the University of Vienna. This research has made use of NASA’s Astrophysics Data System Bibliographic Services. JB acknowledges support by NSF grant AST-1518294 and HST grant GO-13295.001-A. JS acknowledges support by NSF grant AST-1514763 and a Packard Fellowship.

## References

Battaglia, G., Tolstoy, E., Helmi, A., et al. 2006, *A&A*, 459, 423  
 Battistini, C. & Bensby, T. 2015, *A&A*, 577, A9  
 Bensby, T., Feltzing, S., & Lundström, I. 2003, *A&A*, 410, 527  
 Bensby, T., Feltzing, S., & Oey, M. S. 2014, *A&A*, 562, A71  
 Bergemann, M. & Gehren, T. 2008, *A&A*, 492, 823  
 Bressan, A., Marigo, P., Girardi, L., et al. 2012, *MNRAS*, 427, 127  
 Brodie, J. P. & Huchra, J. P. 1991, *ApJ*, 379, 157  
 Brooks, R. S., Wilson, C. D., & Harris, W. E. 2004, *AJ*, 128, 237  
 Cabrera-Ziri, I., Lardo, C., Davies, B., et al. 2016, *MNRAS*, 460, 1869  
 Carretta, E., Bragaglia, A., Gratton, R., & Lucatello, S. 2009, *A&A*, 505, 139  
 Castelli, F. & Hubrig, S. 2004, *A&A*, 425, 263

Chandar, R., Bianchi, L., Ford, H. C., & Sarajedini, A. 2002, *ApJ*, 564, 712  
 Chiappini, C., Matteucci, F., & Romano, D. 2001, *ApJ*, 554, 1044  
 Christian, C. A. & Schommer, R. A. 1982, *ApJS*, 49, 405  
 Cohen, J., Huang, W., & Kirby, E. 2011, *ApJ*, 740, 60  
 Cohen, J. G. 1978, *ApJ*, 223, 487  
 Cohen, J. G. & Huang, W. 2009, *ApJ*, 701, 1053  
 Cohen, J. G. & Huang, W. 2010, *ApJ*, 719, 931  
 Cohen, J. G. & Kirby, E. N. 2012, *ApJ*, 760, 86  
 Coleman, M. G. & de Jong, J. T. A. 2008, *ApJ*, 685, 933  
 Colucci, J. & Bernstein, R. 2011, *EAS Publications Series*, 48, 275  
 Colucci, J. E., Bernstein, R. A., Cameron, S., McWilliam, A., & Cohen, J. G. 2009, *ApJ*, 704, 385  
 Colucci, J. E., Bernstein, R. A., & Cohen, J. G. 2014, *ApJ*, 797, 116  
 Colucci, J. E., Bernstein, R. A., & McWilliam, A. 2017, *ApJ*, 834, 105  
 Conroy, C., Graves, G. J., & van Dokkum, P. G. 2014, *ApJ*, 780, 33  
 Crnojević, D., Ferguson, A. M. N., Irwin, M. J., et al. 2014, *MNRAS*, 445, 3862  
 Da Costa, G. S. & Mould, J. R. 1988, *ApJ*, 334, 159  
 de Boer, T. J. L., Tolstoy, E., Hill, V., et al. 2012, *A&A*, 544, A73  
 Dotter, A., Chaboyer, B., Jevremović, D., et al. 2007, *AJ*, 134, 376  
 Edvardsson, B., Andersen, J., Gustafsson, B., et al. 1993, *A&A*, 275, 101  
 Feast, M. W., Whitelock, P. A., Menzies, J. W., & Matsunaga, N. 2012, *MNRAS*, 421, 2998  
 Fishlock, C. K., Yong, D., Karakas, A. I., et al. 2017, *MNRAS*, 466, 4672  
 Forbes, D. A., Brodie, J. P., & Larsen, S. S. 2001, *ApJ*, 556, L83  
 Forbes, D. A. & Forte, J. C. 2001, *MNRAS*, 322, 257  
 Forte, J. C., Strom, S. E., & Strom, K. M. 1981, *ApJ*, 245, L9  
 Freeman, K. & Bland-Hawthorn, J. 2002, *ARA&A*, 40, 487  
 Fulbright, J. P. 2000, *AJ*, 120, 1841  
 Gazak, J. Z., Davies, B., Bastian, N., et al. 2014, *ApJ*, 787, 142  
 Geha, M., van der Marel, R. P., Guhathakurta, P., et al. 2010, *ApJ*, 711, 361  
 Geha, M., Weisz, D., Grocholski, A., et al. 2015, *ApJ*, 811, 114  
 Gratton, R. G., Carretta, E., & Bragaglia, A. 2012, *A&AR*, 20, 1  
 Gratton, R. G., Carretta, E., Eriksson, K., & Gustafsson, B. 1999, *A&A*, 350, 955  
 Harris, W. E. 1996, *AJ*, 112, 1487  
 Harris, W. E. & Harris, G. L. H. 2002, *AJ*, 123, 3108  
 Harris, W. E., Harris, G. L. H., & Alessi, M. 2013, *ApJ*, 772, 82  
 Harris, W. E., Harris, G. L. H., Layden, A. C., & Wehner, E. M. H. 2007, *ApJ*, 666, 903  
 Hasselquist, S., Shetrone, M., Smith, V., et al. 2017, *ApJ*, 845, 162  
 Helmi, A. 2008, *A&AR*, 15, 145  
 Hendricks, B., Boeche, C., Johnson, C. I., et al. 2016, *A&A*, 585, A86  
 Hernandez, S., Larsen, S., Trager, S., Groot, P., & Kaper, L. 2017, *A&A*, 603, A119  
 Hernandez, S., Larsen, S., Trager, S., Kaper, L., & Groot, P. 2018, *MNRAS*, 473, 826  
 Ho, N., Geha, M., Tollerud, E. J., et al. 2014, *ApJ*, 798, 77  
 Homma, H., Murayama, T., Kobayashi, M. A. R., & Taniguchi, Y. 2015, *ApJ*, 799, 230  
 Hoyle, F. 1954, *ApJS*, 1, 121  
 Hubble, E. P. 1925, *ApJ*, 62, 409  
 Huxor, A., Ferguson, A., Veljanoski, J., Mackey, D., & Tanvir, N. 2013, *MNRAS*, 429, 1039  
 Hwang, N., Lee, M. G., Lee, J. C., et al. 2011, *ApJ*, 738, 58  
 Ishigaki, M. N., Aoki, W., & Chiba, M. 2013, *ApJ*, 771, 67  
 Johnson, L. C., Seth, A. C., Dalcanton, J. J., et al. 2017, *ApJ*, 839, 14  
 Kennicutt, J. 1998, *ApJ*, 498, 541  
 Kissler-Patig, M., Brodie, J. P., & Minniti, D. 2002, *A&A*, 391, 441  
 Kobayashi, C. & Nakasato, N. 2011, *ApJ*, 729, 16  
 Kobayashi, C., Umeda, H., Nomoto, K., Tominaga, N., & Ohkubo, T. 2006, *ApJ*, 653, 1145  
 Kramida, A., Ralchenko, Y., & Reader, J. 2013, *NIST Atomic Spectra Database*  
 Kuntschner, H. 2000, *MNRAS*, 315, 184  
 Lamers, H. J. G. L. M., Kruijssen, J. M. D., Bastian, N., et al. 2017, *A&A*, 606, A85  
 Lanfranchi, G. A., Matteucci, F., & Cescutti, G. 2006, *A&A*, 453, 67  
 Lardo, C., Battaglia, G., Pancino, E., et al. 2016, *A&A*, 585, A70  
 Lardo, C., Davies, B., Kudritzki, R.-P., et al. 2015, *ApJ*, 812, 160  
 Larsen, S. S. 2009, *A&A*, 494, 539  
 Larsen, S. S., Brodie, J. P., Forbes, D. A., & Strader, J. 2014a, *A&A*, 565, A98  
 Larsen, S. S., Brodie, J. P., Grundahl, F., & Strader, J. 2014b, *ApJ*, 797, 15  
 Larsen, S. S., Brodie, J. P., Sarajedini, A., & Huchra, J. P. 2002, *AJ*, 124, 2615  
 Larsen, S. S., Brodie, J. P., & Strader, J. 2012a, *A&A*, 546, A53  
 Larsen, S. S., Brodie, J. P., & Strader, J. 2017, *A&A*, 601, A96  
 Larsen, S. S., Origlia, L., Brodie, J., & Gallagher, J. S. 2008, *MNRAS*, 383, 263  
 Larsen, S. S., Origlia, L., Brodie, J. P., & Gallagher, J. S. 2006, *MNRAS*, 368, L10  
 Larsen, S. S., Strader, J., & Brodie, J. P. 2012b, *A&A*, 544, L14  
 Laverick, M., Lobel, A., Merle, T., et al. 2017, *A&A*, arXiv prep, 1712.07678  
 Lee, H., Skillman, E. D., & Venn, K. A. 2006, *ApJ*, 642, 813

- Lemasle, B., de Boer, T., Hill, V., et al. 2014, A&A, 572, A88
- Letarte, B., Hill, V., Jablonka, P., et al. 2006, A&A, 453, 547
- Letarte, B., Hill, V., Tolstoy, E., et al. 2010, A&A, 523, A17
- Luck, R. E. & Bond, H. E. 1981, ApJ, 244, 919
- Martell, S., Shetrone, M., Lucatello, S., et al. 2016, ApJ, 825, 146
- Martell, S. L., Smolinski, J. P., Beers, T. C., & Grebel, E. K. 2011, A&A, 534, A136
- Matteucci, F. 2001, The chemical evolution of the Galaxy (Dordrecht: Kluwer Academic Publishers)
- Matteucci, F. & Brocato, E. 1990, ApJ, 365, 539
- Matteucci, F. & Greggio, L. 1986, A&A, 154, 279
- McConnachie, A. W. 2012, AJ, 144, 4
- McWilliam, A. 1997, ARA&A, 35, 503
- McWilliam, A. 1998, AJ, 115, 1640
- McWilliam, A., Wallerstein, G., & Mottini, M. 2013, ApJ, 778, 149
- Mucciarelli, A., Bellazzini, M., Ibata, R., et al. 2012, MNRAS, 426, 2889
- Nissen, P. E., Chen, Y. Q., Schuster, W. J., & Zhao, G. 2000, A&A, 353, 722
- Nissen, P. E. & Schuster, W. J. 1997, A&A, 326, 751
- Nissen, P. E. & Schuster, W. J. 2010, A&A, 511, L10
- Ocvirk, P., Pichon, C., Lancon, A., & Thiebaud, E. 2006, MNRAS, 365, 46
- Pagel, B. E. J. & Tautvaisiene, G. 1995, MNRAS, 276, 505
- Patrick, L. R., Evans, C. J., Davies, B., et al. 2015, ApJ, 803, 14
- Payne, C. H. 1925, PhD thesis, Harvard
- Peimbert, M. & Spinrad, H. 1970, A&A, 7, 311
- Pilachowski, C. A., Leep, E. M., & Wallerstein, G. 1980, ApJ, 236, 508
- Pritzl, B. J., Venn, K. A., & Irwin, M. 2005, AJ, 130, 2140
- Reddy, B. E., Tomkin, J., Lambert, D. L., & Prieto, C. A. 2003, MNRAS, 340, 304
- Romano, D. & Starkenburg, E. 2013, MNRAS, 434, 471
- Sakari, C. M., Shetrone, M., Venn, K., McWilliam, A., & Dotter, A. 2013, MNRAS, 434, 358
- Sakari, C. M., Venn, K. A., Mackey, D., et al. 2015, MNRAS, 448, 1314
- Salpeter, E. E. 1955, ApJ, 121, 161
- Sarajedini, A., Barker, M. K., Geisler, D., Harding, P., & Schommer, R. 2006, AJ, 132, 1361
- Sarajedini, A., Bedin, L. R., Chaboyer, B., et al. 2007, AJ, 133, 1658
- Sarajedini, A., Geisler, D., Harding, P., & Schommer, R. 1998, ApJ, 508, L37
- Sarajedini, A., Geisler, D., Schommer, R., & Harding, P. 2000, AJ, 120, 2437
- Sbordone, L., Bonifacio, P., Buonanno, R., et al. 2007, A&A, 465, 815
- Schuster, W. J., Moreno, E., Nissen, P. E., & Pichardo, B. 2012, A&A, 538, A21
- Sharina, M. & Davoust, E. 2009, A&A, 497, 65
- Sharina, M. E., Chandar, R., Puzia, T. H., Goudfrooij, P., & Davoust, E. 2010, MNRAS, 405, 839
- Shetrone, M., Venn, K. A., Tolstoy, E., et al. 2003, AJ, 125, 684
- Snedden, C., Kraft, R. P., Shetrone, M. D., et al. 1997, AJ, 114, 1964
- Snedden, C., Lambert, D. L., & Whitaker, R. W. 1979, ApJ, 234, 964
- Suda, T., Hidaka, J., Aoki, W., et al. 2017, Publications of the Astronomical Society of Japan, 69, 76
- Swan, J., Cole, A. A., Tolstoy, E., & Irwin, M. J. 2016, MNRAS, 456, 4315
- Thomas, D., Maraston, C., Bender, R., & de Oliveira, C. M. 2005, ApJ, 621, 673
- Tinsley, B. M. 1979, ApJ, 229, 1046
- Tissera, P. B., White, S. D. M., & Scannapieco, C. 2012, MNRAS, 420, 255
- Tolstoy, E., Hill, V., & Tosi, M. 2009, ARA&A, 47, 371
- Trager, S. C., Faber, S. M., Worthey, G., & González, J. J. 2000, AJ, 120, 165
- Vargas, L. C., Geha, M. C., & Tollerud, E. J. 2014, ApJ, 790, 73
- Veljanoski, J., Ferguson, A. M. N., Huxor, A. P., et al. 2013, MNRAS, 435, 3654
- Veljanoski, J., Ferguson, A. M. N., Mackey, A. D., et al. 2015, MNRAS, 452, 320
- Venn, K. A., Irwin, M., Shetrone, M. D., et al. 2004, AJ, 128, 1177
- Venn, K. A., Lennon, D. J., Kaufer, A., et al. 2001, ApJ, 547, 765
- Villanova, S., Geisler, D., Carraro, G., Bidin, C. M., & Munoz, C. 2013, ApJ, 778, 186
- Vincenzo, F., Matteucci, F., Recchi, S., et al. 2015, MNRAS, 449, 1327
- Vogt, S. S., Allen, S. L., Bigelow, B. C., et al. 1994, Proc. SPIE, 2198, 362
- Worthey, G., Faber, S. M., & Gonzalez, J. J. 1992, ApJ, 398, 69

**Appendix A: Individual abundance measurements**

**Appendix B: Abundances based on Kurucz line list**

**Table B.1.** Abundance measurements.

	[Fe/H] rms <sub>w</sub> (N)	[Na/Fe] rms <sub>w</sub> (N)	[Mg/Fe] rms <sub>w</sub> (N)	[Ca/Fe] rms <sub>w</sub> (N)	[Sc/Fe] rms <sub>w</sub> (N)	[Ti/Fe] rms <sub>w</sub> (N)	[Cr/Fe] rms <sub>w</sub> (N)	[Mn/Fe] rms <sub>w</sub> (N)	[Ni/Fe] rms <sub>w</sub> (N)	[Ba/Fe] rms <sub>w</sub> (N)
NGC 147 HII	−1.576	+0.428	+0.285	+0.291	+0.267	+0.250	−0.068	−0.018	+0.029	−0.158
	0.225 (24)	0.086 <sup>a</sup> (1)	0.207 (4)	0.195 (5)	0.254 (5)	0.266 (7)	0.127 (7)	0.298 (2)	0.425 (11)	0.391 (3)
NGC 147 HIII	−2.478	+0.656	+0.245	+0.451	+0.267	+0.426	−0.171	+0.233	−0.407	−0.356
	0.162 (24)	0.090 <sup>a</sup> (1)	0.123 (4)	0.055 (5)	0.375 (5)	0.125 (7)	0.288 (8)	0.278 (2)	0.636 (6)	0.121 (4)
NGC 147 PA-1	−2.379	+0.577	+0.346	+0.264	+0.062	+0.380	−0.010	+0.067	+0.070	+0.114
	0.127 (23)	0.150 <sup>a</sup> (1)	0.127 (5)	0.217 (8)	0.362 (5)	0.168 (9)	0.331 (10)	0.080 (1)	0.106 (4)	0.187 (4)
NGC 147 PA-2	−2.018	+0.349	+0.462	+0.400	+0.216	+0.374	+0.067	−0.213	+0.019	+0.362
	0.100 (27)	0.080 <sup>a</sup> (1)	0.090 (5)	0.132 (8)	0.215 (6)	0.135 (9)	0.197 (10)	0.081 (2)	0.256 (11)	0.101 (4)
NGC 147 SD7	−2.049	−0.199	+0.511	+0.368	+0.070	+0.366	+0.080	−0.343	+0.148	+0.334
	0.115 (26)	0.165 <sup>a</sup> (1)	0.309 (5)	0.128 (8)	0.248 (6)	0.140 (10)	0.239 (11)	0.126 (2)	0.326 (13)	0.338 (4)
NGC 6822 SC6	−1.833	+0.301	+0.348	+0.269	+0.186	+0.262	−0.013	−0.381	−0.079	+0.288
	0.078 (27)	0.096 <sup>a</sup> (1)	0.188 (6)	0.165 (8)	0.168 (7)	0.107 (9)	0.170 (11)	0.045 (2)	0.236 (12)	0.078 (4)
NGC 6822 SC7	−1.286	−0.366	−0.129	+0.058	−0.218	+0.010	−0.093	−0.292	−0.199	+0.187
	0.091 (26)	0.071 <sup>a</sup> (1)	0.097 (5)	0.154 (8)	0.154 (7)	0.121 (10)	0.122 (11)	0.061 (2)	0.192 (14)	0.069 (4)
M33 H38	−1.207	+0.012	+0.038	+0.303	+0.200	+0.424	+0.170	−0.343	+0.161	+0.589
	0.195 (23)	0.096 <sup>a</sup> (1)	0.450 (2)	0.343 (8)	0.251 (4)	0.406 (12)	0.223 (7)	0.275 (2)	0.405 (12)	0.122 (4)
M33 M9	−1.766	+0.225	+0.019	+0.308	+0.214	+0.340	+0.008	−0.313	−0.097	+0.600
	0.095 (26)	0.080 <sup>a</sup> (1)	0.118 (3)	0.176 (9)	0.221 (6)	0.154 (12)	0.097 (9)	0.060 (2)	0.237 (11)	0.132 (4)
M33 R12	−0.960	+0.106	+0.291	+0.324	+0.234	+0.268	+0.058	−0.107	+0.045	+0.374
	0.078 (26)	0.043 <sup>a</sup> (1)	0.209 (3)	0.133 (9)	0.122 (6)	0.122 (12)	0.181 (11)	0.129 (2)	0.260 (13)	0.164 (4)
M33 U49	−1.481	+0.100	+0.347	+0.211	+0.402	+0.402	+0.127	+0.004	+0.026	+0.667
	0.126 (26)	0.116 <sup>a</sup> (1)	0.218 (3)	0.260 (8)	0.273 (5)	0.250 (11)	0.241 (10)	0.126 (2)	0.330 (10)	0.137 (3)
WLM GC	−1.959	+0.238	+0.118	+0.273	+0.306	+0.160	−0.114	−0.432	+0.045	−0.054
	0.094 (10)	0.141 <sup>a</sup> (1)	0.126 (5)	0.104 (6)	0.127 (6)	0.159 (9)	0.174 (6)	0.143 (2)	0.319 (13)	0.124 (4)
Fornax 3	−2.354	+0.009	+0.032	+0.259	+0.250	+0.297	−0.151	−0.420	−0.139	+0.545
	0.062 (10)	0.165 <sup>a</sup> (1)	0.180 (5)	0.196 (8)	0.135 (6)	0.102 (9)	0.108 (6)	0.193 (2)	0.268 (12)	0.069 (4)
Fornax 4	−1.413	−0.148	+0.038	+0.099	+0.048	+0.101	−0.060	−0.299	−0.179	+0.154
	0.031 (10)	0.046 <sup>a</sup> (1)	0.121 (5)	0.149 (8)	0.062 (6)	0.096 (9)	0.113 (6)	0.052 (2)	0.182 (15)	0.042 (4)
Fornax 5	−2.137	+0.508	+0.249	+0.300	+0.085	+0.245	+0.080	−0.363	+0.031	−0.124
	0.087 (10)	0.090 <sup>a</sup> (1)	0.182 (5)	0.174 (8)	0.217 (6)	0.080 (9)	0.168 (6)	0.076 (1)	0.318 (14)	0.112 (4)

**Notes.** For each cluster, the first line gives the average abundance ratio and the second line gives the weighted rms and number of individual measurements. (a): For [Na/Fe] we list the errors on the individual measurements of the doublet at 5683/5688 Å.



**Table A.1.** Individual abundance measurements for NGC 147 Hodge II

Wavelength [Å]	Value	Error
[Fe/H]		
4209.7–4284.4	−1.853	0.036
4260.4–4336.0	...	
4312.4–4388.9	...	
4365.6–4443.1	−1.034	0.041
4420.1–4498.6	−1.663	0.070
4476.1–4555.6	−1.363	0.085
4533.4–4614.0	−1.724	0.110
4592.3–4674.0	−1.312	0.081
4652.7–4735.5	−1.473	0.106
4714.7–4798.6	−1.243	0.081
4778.4–4863.5	−1.413	0.106
4843.9–4930.1	−1.503	0.056
4911.1–4998.6	−1.243	0.066
5096.0–5141.5	−1.783	0.060
5124.7–5216.1	−1.983	0.051
5200.0–5292.8	−1.543	0.045
5277.6–5371.8	−1.692	0.061
5357.6–5453.2	−1.932	0.051
5440.0–5537.1	−1.644	0.055
5525.0–5623.6	−1.373	0.056
5612.7–5712.9	−1.293	0.061
5703.2–5805.0	−1.814	0.126
5796.7–5900.2	−1.602	0.096
5893.3–5998.5	−1.312	0.060
5993.2–6100.2	−1.483	0.075
6096.5–6205.3	−1.312	0.060
[Na/Fe]		
5677.0–5695.0	+0.398	0.085
6149.0–6166.0	+0.478	0.175
[Mg/Fe]		
4347.0–4357.0	...	
4565.0–4576.0	+0.088	0.256
4700.0–4707.0	−0.232	0.346
5523.0–5531.5	+0.268	0.266
5525.0–5531.5	+0.407	0.155
5705.0–5715.0	< −0.343	
[Ca/Fe]		
4222.0–4232.0	...	
4280.0–4320.0	−0.112	0.105
4420.0–4460.0	+0.818	0.180
4575.0–4591.0	−0.112	0.175
4873.0–4883.0	...	
5259.0–5268.0	+0.519	0.111
5580.0–5610.0	+0.298	0.071
6100.0–6175.0	+0.258	0.060
[Sc/Fe]		
4290.0–4330.0	...	
4350.0–4375.0	+0.737	0.300
4375.0–4425.0	−0.193	0.221
4425.0–4440.0	...	
4665.0–4675.0	+0.159	0.405
5521.0–5531.0	−0.852	0.396
5638.0–5690.0	+0.197	0.085
[Ti/Fe]		
4292.0–4320.0	...	
4386.0–4417.0	...	
4440.0–4475.0	+0.417	0.115
4533.0–4574.0	+0.327	0.110
4587.0–4593.0	...	

Table A.1. continued.

Wavelength [Å]	Value	Error
4653.0–4715.0	+0.319	0.146
4750.0–4785.0	+0.407	0.150
4785.0–4850.0	+0.229	0.145
5152.0–5160.0	−0.342	0.275
[Cr/Fe]		
4250.0–4275.0	...	
4262.0–4292.0	...	
4350.0–4375.0	−0.882	0.360
4370.0–4400.0	...	
4520.0–4545.0	−0.462	0.435
4540.0–4600.0	+0.098	0.126
4600.0–4660.0	+0.107	0.096
5235.0–5280.0	−0.171	0.096
5280.0–5330.0	−0.361	0.126
5342.0–5351.0	−0.103	0.161
5407.0–5413.0	−0.691	0.286
[Mn/Fe]		
4750.0–4790.0	−0.442	0.145
6010.0–6030.0	+0.097	0.141
[Ni/Fe]		
4600.0–4610.0	+0.849	0.216
4644.0–4654.0	+0.298	0.486
4681.0–4691.0	...	
4709.0–4719.0	−0.022	0.321
4824.0–4835.0	+0.098	0.271
4899.0–4909.0	−0.322	0.341
4931.0–4942.0	+0.639	0.216
4975.0–4985.0	+0.497	0.191
5098.0–5108.0	+0.088	0.166
5141.0–5151.0	...	
5472.0–5482.0	+0.178	0.185
5707.0–5717.0	−0.262	0.296
6103.0–6113.0	−0.193	0.295
6172.0–6182.0	< −0.213	
[Ba/Fe]		
4551.0–4560.0	...	
4929.0–4939.0	−0.261	0.205
5849.0–5859.0	+0.379	0.215
6135.0–6145.0	−0.672	0.205

**Table A.2.** Individual abundance measurements for NGC 147 Hodge III

Wavelength [Å]	Value	Error
[Fe/H]		
4209.8–4284.4	−2.582	0.061
4260.5–4336.0	−2.123	0.056
4312.4–4388.9	−2.513	0.106
4365.7–4443.1	−2.502	0.066
4420.2–4498.7	−2.582	0.066
4476.1–4555.6	−2.482	0.051
4533.5–4614.1	−2.513	0.085
4592.4–4674.0	−2.292	0.066
4652.8–4735.5	−2.433	0.110
4714.8–4798.7	−2.711	0.175
4778.5–4863.5	−1.991	0.155
4843.9–4930.2	−2.572	0.051
4911.2–4998.7	−2.611	0.051
5095.3–5141.6	−2.172	0.051
5124.8–5216.1	−2.452	0.030
5200.1–5292.8	−2.412	0.036
5277.7–5371.8	−2.442	0.035
5357.7–5453.2	−2.523	0.035
5440.1–5537.1	−2.813	0.056
5525.1–5623.6	−2.711	0.055
5612.8–5712.9	−2.691	0.110
5703.3–5805.1	−2.643	0.391
5796.8–5900.2	...	
5893.4–5998.6	−2.523	0.170
5993.3–6100.2	−2.711	0.150
6096.6–6205.4	−2.502	0.075
[Na/Fe]		
5677.0–5695.0	+0.648	0.091
6149.0–6166.0	...	
[Mg/Fe]		
4347.0–4357.0	+0.089	0.155
4565.0–4576.0	+0.408	0.206
4700.0–4707.0	+0.308	0.101
5523.0–5531.5	+0.008	0.120
5705.0–5715.0	...	
[Ca/Fe]		
4222.0–4232.0	+0.418	0.120
4280.0–4320.0	+0.599	0.091
4420.0–4460.0	+0.328	0.071
4575.0–4591.0	+0.838	0.101
4873.0–4883.0	...	
5259.0–5268.0	...	
5580.0–5610.0	+0.508	0.046
6100.0–6175.0	+0.347	0.040
[Sc/Fe]		
4290.0–4330.0	+0.669	0.120
4350.0–4375.0	+0.508	0.220
4375.0–4425.0	−0.402	0.215
4425.0–4440.0	...	
4665.0–4675.0	< −0.102	
5521.0–5531.0	−0.333	0.266
5638.0–5690.0	+0.028	0.131
[Ti/Fe]		
4292.0–4320.0	+0.628	0.071
4386.0–4420.0	+0.498	0.085
4440.0–4474.0	+0.267	0.091
4533.0–4574.0	+0.318	0.061
4587.0–4593.0	< −0.252	
4653.0–4715.0	+0.838	0.075

Table A.2. continued.

Wavelength [Å]	Value	Error
4750.0–4785.0	+0.399	0.165
4785.0–4850.0	+0.610	0.120
4982.0–5000.0	< −0.253	
5152.0–5160.0	+0.347	0.210
[Cr/Fe]		
4250.0–4275.0	−0.492	0.185
4262.0–4292.0	+0.298	0.150
4350.0–4375.0	...	
4370.0–4400.0	...	
4520.0–4545.0	...	
4540.0–4600.0	< −0.242	
4600.0–4660.0	−0.292	0.185
5235.0–5280.0	−0.402	0.230
5280.0–5330.0	−0.312	0.276
5342.0–5351.0	−0.192	0.165
5407.0–5413.0	−0.452	0.216
[Mn/Fe]		
4750.0–4790.0	−0.111	0.126
6010.0–6030.0	+0.487	0.120
[Ni/Fe]		
4600.0–4610.0	...	
4644.0–4654.0	−0.002	1.026
4681.0–4691.0	< +0.507	
4709.0–4719.0	+0.789	0.160
4824.0–4835.0	+0.437	0.270
4899.0–4909.0	+0.079	0.525
4931.0–4942.0	...	
4975.0–4985.0	...	
5098.0–5108.0	...	
5141.0–5151.0	< +0.157	
5472.0–5482.0	−0.312	0.085
5707.0–5717.0	< −0.233	
6103.0–6113.0	< +0.187	
6172.0–6182.0	< +0.607	
[Ba/Fe]		
4551.0–4560.0	−0.341	0.230
4929.0–4939.0	−0.291	0.145
5849.0–5859.0	−0.102	0.221
6135.0–6145.0	−0.252	0.115

**Table A.3.** Individual abundance measurements for NGC 147 PA1

Wavelength [Å]	Value	Error
[Fe/H]		
4209.9–4284.6	−2.578	0.051
4260.6–4336.2	−1.969	0.045
4312.6–4389.1	−2.269	0.071
4365.8–4443.3	−2.218	0.051
4420.4–4498.9	−2.439	0.051
4476.3–4555.8	−2.359	0.061
4533.6–4614.2	−2.478	0.096
4592.5–4674.2	−2.218	0.056
4652.9–4735.7	−2.748	0.175
4714.9–4798.9	−2.237	0.081
4778.6–4863.7	...	
4844.1–4930.4	−2.408	0.051
4911.3–4998.9	−2.418	0.045
5095.7–5141.8	−2.218	0.051
5124.9–5216.3	−2.368	0.030
5200.3–5293.0	−2.368	0.036
5277.9–5372.0	−2.398	0.041
5357.8–5453.4	−2.449	0.030
5440.2–5537.3	−2.478	0.041
5525.2–5623.9	−2.498	0.051
5612.9–5713.1	−2.327	0.080
5703.4–5805.3	−3.097	5.205
5796.9–5900.4	...	
5893.5–5998.8	...	
5993.4–6100.4	−2.408	0.111
6096.8–6205.6	−2.498	0.070
[Na/Fe]		
5677.0–5695.0	+0.552	0.146
6149.0–6166.0	< +0.701	
[Mg/Fe]		
4347.0–4357.0	+0.032	0.180
4565.0–4576.0	+0.502	0.160
4700.0–4707.0	+0.172	0.101
5523.0–5531.5	+0.392	0.126
5705.0–5715.0	+0.603	0.215
[Ca/Fe]		
4222.0–4232.0	−0.079	0.115
4280.0–4320.0	−0.279	0.115
4420.0–4460.0	+0.423	0.075
4575.0–4591.0	+0.043	0.200
4873.0–4883.0	+0.292	0.351
5259.0–5268.0	+0.672	0.080
5580.0–5610.0	+0.231	0.060
6100.0–6175.0	+0.162	0.041
[Sc/Fe]		
4290.0–4330.0	+0.363	0.131
4350.0–4375.0	+0.192	0.215
4375.0–4425.0	−0.627	0.221
4425.0–4440.0	...	
4665.0–4675.0	< −0.219	
5521.0–5531.0	−0.627	0.415
5638.0–5690.0	−0.218	0.196
[Ti/Fe]		
4292.0–4320.0	+0.543	0.075
4386.0–4417.0	+0.272	0.090
4440.0–4475.0	+0.382	0.070
4533.0–4574.0	+0.382	0.075
4587.0–4593.0	−0.138	0.271
4653.0–4715.0	−0.008	0.146
4750.0–4785.0	+0.532	0.105



Table A.3. continued.

Wavelength [Å]	Value	Error
4785.0–4850.0	+0.252	0.170
5152.0–5160.0	−0.008	0.230
[Cr/Fe]		
4250.0–4275.0	−0.738	0.181
4262.0–4292.0	−0.837	0.161
4350.0–4375.0	−0.938	0.775
4370.0–4400.0	...	
4520.0–4545.0	+0.672	0.126
4540.0–4600.0	+0.133	0.101
4600.0–4660.0	−0.048	0.081
5235.0–5280.0	−0.369	0.136
5280.0–5330.0	+0.143	0.090
5342.0–5351.0	−0.148	0.110
5407.0–5413.0	+0.231	0.096
[Mn/Fe]		
4750.0–4790.0	+0.032	0.080
6010.0–6030.0	< −0.108	
[Ni/Fe]		
4600.0–4610.0	...	
4644.0–4654.0	< +0.061	
4681.0–4691.0	< +0.331	
4709.0–4719.0	< −0.199	
4824.0–4835.0	< +0.312	
4899.0–4909.0	+0.082	0.240
4931.0–4942.0	< +0.322	
4975.0–4985.0	−0.199	0.356
5098.0–5108.0	+0.021	0.200
5141.0–5151.0	...	
5472.0–5482.0	−0.578	0.145
5707.0–5717.0	< −0.399	
6103.0–6113.0	...	
6172.0–6182.0	< +0.312	
[Ba/Fe]		
4551.0–4560.0	+0.141	0.185
4929.0–4939.0	+0.121	0.136
5849.0–5859.0	−0.078	0.196
6135.0–6145.0	+0.322	0.120

**Table A.4.** Individual abundance measurements for NGC 147 PA2

Wavelength [Å]	Value	Error
[Fe/H]		
4209.9–4284.6	−2.119	0.035
4260.6–4336.2	−1.908	0.041
4312.6–4389.1	−1.799	0.046
4365.8–4443.3	−2.170	0.036
4420.4–4498.9	−2.050	0.040
4476.3–4555.8	−1.960	0.041
4533.6–4614.2	−2.079	0.051
4592.5–4674.2	−1.960	0.041
4652.9–4735.7	−1.999	0.045
4714.9–4798.9	−2.009	0.051
4778.6–4863.7	−2.189	0.151
4844.1–4930.4	−2.019	0.036
4911.3–4998.9	−2.138	0.025
4980.5–5023.7	−1.918	0.045
5088.8–5141.8	−1.848	0.036
5124.9–5216.3	−1.939	0.020
5200.3–5293.0	−2.029	0.021
5277.9–5372.1	−1.999	0.030
5357.8–5453.4	−2.079	0.020
5440.2–5537.4	−2.019	0.025
5525.2–5623.9	−1.908	0.026
5612.9–5713.2	−2.099	0.041
5703.5–5805.3	−2.009	0.075
5796.9–5900.4	−2.559	0.156
5893.6–5998.8	−2.299	0.075
5993.4–6100.5	−1.899	0.045
6096.8–6205.6	−2.029	0.041
[Na/Fe]		
5677.0–5695.0	+0.343	0.085
6149.0–6166.0	+0.104	0.500
[Mg/Fe]		
4347.0–4357.0	+0.023	0.156
4565.0–4576.0	+0.413	0.131
4700.0–4707.0	+0.564	0.110
5523.0–5531.5	+0.483	0.091
5705.0–5715.0	+0.283	0.105
[Ca/Fe]		
4222.0–4232.0	+0.052	0.085
4280.0–4320.0	+0.362	0.075
4420.0–4460.0	+0.483	0.066
4575.0–4591.0	+0.152	0.090
4873.0–4883.0	+0.433	0.165
5259.0–5268.0	+0.543	0.061
5580.0–5610.0	+0.514	0.036
6100.0–6175.0	+0.313	0.030
[Sc/Fe]		
4290.0–4330.0	+0.623	0.105
4350.0–4375.0	−0.087	0.206
4375.0–4425.0	+0.184	0.105
4425.0–4440.0	...	
4665.0–4675.0	+0.023	0.175
5521.0–5531.0	−0.216	0.105
5638.0–5690.0	+0.113	0.056
[Ti/Fe]		
4292.0–4320.0	+0.373	0.066
4386.0–4417.0	+0.442	0.056
4440.0–4475.0	+0.164	0.060
4533.0–4574.0	+0.442	0.051
4587.0–4593.0	+0.824	0.115
4653.0–4715.0	+0.423	0.060

Table A.4. continued.

Wavelength [Å]	Value	Error
4750.0–4785.0	+0.272	0.096
4785.0–4850.0	+0.383	0.066
5152.0–5160.0	+0.283	0.110
[Cr/Fe]		
4250.0–4275.0	+0.133	0.131
4262.0–4292.0	+0.313	0.090
4350.0–4375.0	−0.328	0.166
4370.0–4400.0	−0.177	0.245
4520.0–4545.0	< −0.427	
4540.0–4600.0	−0.126	0.100
4600.0–4660.0	−0.017	0.056
5235.0–5280.0	−0.057	0.066
5280.0–5330.0	−0.148	0.060
5342.0–5351.0	+0.084	0.071
5407.0–5413.0	+0.442	0.096
[Mn/Fe]		
4750.0–4790.0	−0.217	0.081
6010.0–6030.0	−0.608	0.300
[Ni/Fe]		
4600.0–4610.0	−0.097	0.321
4644.0–4654.0	+0.174	0.141
4681.0–4691.0	...	
4709.0–4719.0	−0.216	0.131
4824.0–4835.0	−0.046	0.196
4899.0–4909.0	−0.028	0.210
4931.0–4942.0	< −0.088	
4975.0–4985.0	−0.187	0.136
5098.0–5108.0	−0.547	0.320
5141.0–5151.0	+0.073	0.131
5472.0–5482.0	+0.333	0.110
5707.0–5717.0	+0.243	0.085
6103.0–6113.0	−0.616	0.395
6172.0–6182.0	< +0.043	
[Ba/Fe]		
4551.0–4560.0	+0.403	0.106
4929.0–4939.0	+0.373	0.085
5849.0–5859.0	+0.533	0.105
6135.0–6145.0	+0.363	0.085

**Table A.5.** Individual abundance measurements for NGC 147 SD7

Wavelength [Å]	Value	Error
[Fe/H]		
4209.8–4284.4	−2.008	0.036
4260.5–4336.0	−2.239	0.045
4312.5–4388.9	−2.127	0.060
4365.7–4443.1	−2.048	0.036
4420.2–4498.7	−2.037	0.045
4476.2–4555.6	−2.008	0.051
4533.5–4614.1	−2.098	0.051
4592.4–4674.0	−1.988	0.036
4652.8–4735.5	−1.939	0.035
4714.8–4798.7	−1.858	0.046
4778.5–4863.5	−2.098	0.105
4843.9–4930.2	−1.998	0.036
4911.2–4998.7	−1.978	0.025
5095.3–5141.6	−2.398	0.040
5124.8–5216.1	−2.149	0.026
5200.1–5292.8	−2.008	0.025
5277.7–5371.8	−2.239	0.030
5357.7–5453.2	−2.098	0.016
5440.1–5537.1	−1.948	0.030
5525.1–5623.6	−2.107	0.036
5612.8–5712.9	−1.948	0.036
5703.3–5805.0	−2.127	0.115
5796.8–5900.2	−2.298	0.096
5893.4–5998.6	−2.098	0.066
5993.3–6100.2	−2.037	0.045
6096.6–6205.4	−1.907	0.036
[Na/Fe]		
5677.0–5695.0	−0.192	0.166
6149.0–6166.0	+0.427	0.191
[Mg/Fe]		
4347.0–4357.0	−0.332	0.160
4565.0–4576.0	+0.818	0.120
4700.0–4707.0	+0.398	0.085
5523.0–5531.5	+0.908	0.096
5705.0–5715.0	−0.051	0.256
[Ca/Fe]		
4222.0–4232.0	+0.027	0.080
4280.0–4320.0	+0.579	0.096
4420.0–4460.0	+0.149	0.071
4575.0–4591.0	+0.278	0.085
4873.0–4883.0	+0.348	0.145
5259.0–5268.0	+0.448	0.055
5580.0–5610.0	+0.507	0.041
6100.0–6175.0	+0.337	0.030
[Sc/Fe]		
4290.0–4330.0	+0.417	0.091
4350.0–4375.0	+0.048	0.201
4375.0–4425.0	−0.242	0.085
4425.0–4440.0	...	
4665.0–4675.0	−0.042	0.200
5521.0–5531.0	−0.681	0.160
5638.0–5690.0	+0.058	0.075
[Ti/Fe]		
4292.0–4320.0	+0.529	0.071
4386.0–4420.0	+0.378	0.056
4440.0–4474.0	+0.258	0.061
4533.0–4574.0	+0.398	0.055
4587.0–4593.0	−0.452	0.215
4653.0–4715.0	+0.408	0.060
4750.0–4785.0	+0.597	0.071

Table A.5. continued.

Wavelength [Å]	Value	Error
4785.0–4850.0	+0.488	0.076
4982.0–5000.0	+0.629	0.090
5152.0–5160.0	+0.629	0.126
[Cr/Fe]		
4250.0–4275.0	+0.188	0.110
4262.0–4292.0	−0.412	0.160
4350.0–4375.0	−0.752	0.290
4370.0–4400.0	−0.501	0.290
4520.0–4545.0	−0.252	0.266
4540.0–4600.0	−0.161	0.090
4600.0–4660.0	+0.278	0.061
5235.0–5280.0	+0.169	0.060
5280.0–5330.0	−0.291	0.085
5342.0–5351.0	+0.298	0.085
5407.0–5413.0	−0.242	0.101
[Mn/Fe]		
4750.0–4790.0	−0.422	0.081
6010.0–6030.0	−0.351	0.175
[Ni/Fe]		
4600.0–4610.0	−0.183	0.310
4644.0–4654.0	+0.188	0.270
4681.0–4691.0	< +0.178	
4709.0–4719.0	−0.102	0.126
4824.0–4835.0	+0.398	0.110
4899.0–4909.0	+0.718	0.165
4931.0–4942.0	+0.539	0.165
4975.0–4985.0	−0.472	0.215
5098.0–5108.0	+0.159	0.085
5141.0–5151.0	+0.469	0.111
5472.0–5482.0	+0.337	0.101
5707.0–5717.0	−0.542	0.151
6103.0–6113.0	−0.273	0.210
6172.0–6182.0	...	
[Ba/Fe]		
4551.0–4560.0	+0.237	0.115
4929.0–4939.0	−0.251	0.126
5849.0–5859.0	+0.699	0.051
6135.0–6145.0	+0.087	0.090



**Table A.6.** Individual abundance measurements for NGC 6822 SC6

Wavelength [Å]	Value	Error
[Fe/H]		
4206.4–4280.9	−1.919	0.035
4257.0–4332.5	−1.839	0.041
4308.9–4385.4	−1.860	0.045
4362.1–4439.6	−1.850	0.030
4416.6–4495.1	−1.819	0.041
4472.5–4552.0	−1.749	0.045
4529.8–4610.3	−1.789	0.045
4588.6–4670.2	−1.839	0.041
4649.0–4731.7	−1.938	0.051
4711.0–4794.8	−1.938	0.066
4774.6–4859.6	−1.970	0.081
4840.0–4926.2	−1.860	0.035
4907.2–4994.6	−1.860	0.030
4976.3–5020.1	−1.860	0.060
5080.1–5137.4	−1.670	0.041
5120.6–5211.9	−1.789	0.030
5195.9–5288.6	−1.749	0.025
5273.4–5367.5	−1.799	0.036
5353.3–5448.8	−1.868	0.025
5435.6–5532.6	−1.889	0.030
5520.6–5619.1	−1.819	0.045
5608.2–5708.3	−1.889	0.051
5698.6–5800.4	−1.579	0.061
5792.0–5895.5	−1.948	0.096
5888.6–5993.7	−1.909	0.061
5988.4–6095.3	−1.638	0.051
6091.6–6200.4	−1.689	0.046
[Na/Fe]		
5677.0–5695.0	+0.284	0.090
6149.0–6166.0	+0.124	0.461
[Mg/Fe]		
4347.0–4357.0	−0.415	0.190
4565.0–4576.0	−0.006	0.141
4700.0–4707.0	+0.344	0.096
5523.0–5531.5	+0.555	0.150
5525.0–5531.5	+0.414	0.101
5705.0–5715.0	+0.374	0.111
[Ca/Fe]		
4222.0–4232.0	−0.045	0.070
4280.0–4320.0	+0.124	0.085
4420.0–4460.0	+0.273	0.066
4575.0–4591.0	−0.037	0.096
4873.0–4883.0	+0.624	0.175
5259.0–5268.0	+0.424	0.085
5580.0–5610.0	+0.443	0.056
6100.0–6175.0	+0.194	0.041
[Sc/Fe]		
4290.0–4330.0	−0.086	0.120
4350.0–4375.0	+0.014	0.191
4375.0–4425.0	+0.063	0.120
4425.0–4440.0	−0.247	0.696
4665.0–4675.0	−0.286	0.230
5521.0–5531.0	−0.027	0.230
5638.0–5690.0	+0.244	0.066
[Ti/Fe]		
4292.0–4320.0	+0.414	0.061
4386.0–4417.0	+0.344	0.066
4440.0–4475.0	+0.255	0.060
4533.0–4574.0	+0.334	0.045
4587.0–4593.0	+0.175	0.141

Table A.6. continued.

Wavelength [Å]	Value	Error
4653.0–4715.0	+0.124	0.070
4750.0–4785.0	+0.284	0.081
4785.0–4850.0	+0.153	0.085
5152.0–5160.0	+0.353	0.150
[Cr/Fe]		
4250.0–4275.0	−0.247	0.136
4262.0–4292.0	+0.134	0.096
4350.0–4375.0	−0.327	0.155
4370.0–4400.0	−0.166	0.181
4520.0–4545.0	+0.194	0.106
4540.0–4600.0	−0.106	0.075
4600.0–4660.0	−0.096	0.066
5235.0–5280.0	+0.053	0.075
5280.0–5330.0	−0.115	0.066
5342.0–5351.0	−0.086	0.120
5407.0–5413.0	+0.044	0.131
[Mn/Fe]		
4750.0–4790.0	−0.415	0.075
6010.0–6030.0	−0.836	0.461
[Ni/Fe]		
4600.0–4610.0	−0.076	0.210
4644.0–4654.0	−0.106	0.195
4681.0–4691.0	< −0.147	
4709.0–4719.0	+0.085	0.150
4824.0–4835.0	−0.225	0.201
4899.0–4909.0	−0.346	0.251
4931.0–4942.0	−0.337	0.381
4975.0–4985.0	−0.106	0.160
5098.0–5108.0	−0.376	0.175
5141.0–5151.0	−0.355	0.175
5472.0–5482.0	+0.244	0.126
5707.0–5717.0	+0.085	0.120
6103.0–6113.0	−0.056	0.171
6172.0–6182.0	−0.286	0.461
[Ba/Fe]		
4551.0–4560.0	+0.505	0.081
4929.0–4939.0	+0.234	0.120
5849.0–5859.0	+0.305	0.141
6135.0–6145.0	+0.435	0.106

**Table A.7.** Individual abundance measurements for NGC 6822 SC7

Wavelength [Å]	Value	Error
[Fe/H]		
4207.1–4281.6	−1.360	0.018
4257.8–4333.2	−1.418	0.020
4309.7–4386.1	−1.422	0.025
4362.9–4440.3	−1.330	0.021
4417.4–4495.8	−1.251	0.025
4473.3–4552.7	−1.251	0.025
4530.6–4611.1	−1.341	0.030
4589.4–4671.0	−1.289	0.020
4649.8–4732.5	−1.340	0.026
4711.8–4795.6	−1.221	0.030
4775.4–4860.4	−1.189	0.035
4840.8–4927.0	−1.372	0.015
4908.0–4995.5	−1.240	0.020
5092.0–5138.2	−1.171	0.025
5121.5–5212.7	−1.301	0.015
5196.8–5289.4	−1.212	0.015
5274.3–5368.4	−1.197	0.020
5354.2–5449.7	−1.341	0.016
5436.6–5533.6	−1.240	0.016
5521.5–5620.0	−1.279	0.021
5609.1–5709.2	−1.250	0.021
5699.6–5801.3	−1.091	0.029
5793.0–5896.4	−1.371	0.041
5889.6–5994.7	−1.301	0.030
5989.4–6096.3	−1.030	0.026
6092.7–6201.4	−1.086	0.021
[Na/Fe]		
5677.0–5695.0	−0.366	0.070
6149.0–6166.0	−0.590	0.415
[Mg/Fe]		
4347.0–4357.0	−0.799	0.126
4565.0–4576.0	−0.129	0.085
4700.0–4707.0	−0.090	0.071
5523.0–5531.5	−0.048	0.079
5705.0–5715.0	−0.237	0.090
[Ca/Fe]		
4222.0–4232.0	−0.157	0.041
4280.0–4320.0	−0.120	0.066
4420.0–4460.0	+0.128	0.041
4575.0–4591.0	−0.107	0.060
4873.0–4883.0	+0.188	0.131
5259.0–5268.0	+0.212	0.051
5580.0–5610.0	+0.211	0.030
6100.0–6175.0	−0.035	0.026
[Sc/Fe]		
4290.0–4330.0	−0.288	0.080
4350.0–4375.0	−0.209	0.120
4375.0–4425.0	−0.558	0.081
4425.0–4440.0	−0.610	0.340
4665.0–4675.0	−0.452	0.141
5521.0–5531.0	−0.426	0.122
5638.0–5690.0	−0.247	0.041
[Ti/Fe]		
4292.0–4320.0	−0.075	0.051
4386.0–4420.0	+0.049	0.036
4440.0–4474.0	−0.003	0.036
4533.0–4574.0	−0.054	0.035
4587.0–4593.0	+0.528	0.096
4653.0–4715.0	−0.088	0.045
4750.0–4785.0	+0.121	0.056

Table A.7. continued.

Wavelength [Å]	Value	Error
4785.0–4850.0	−0.040	0.055
4982.0–5000.0	−0.028	0.110
5152.0–5160.0	+0.441	0.096
[Cr/Fe]		
4250.0–4275.0	−0.117	0.055
4262.0–4292.0	−0.189	0.060
4350.0–4375.0	−0.097	0.090
4370.0–4400.0	−0.490	0.120
4520.0–4545.0	−0.040	0.056
4540.0–4600.0	−0.134	0.046
4600.0–4660.0	−0.125	0.040
5235.0–5280.0	+0.020	0.035
5280.0–5330.0	−0.122	0.030
5342.0–5351.0	−0.378	0.071
5407.0–5413.0	−0.108	0.085
[Mn/Fe]		
4750.0–4790.0	−0.375	0.045
6010.0–6030.0	−0.419	0.071
[Ni/Fe]		
4600.0–4610.0	−0.288	0.115
4644.0–4654.0	−0.494	0.141
4681.0–4691.0	−0.463	0.155
4709.0–4719.0	−0.220	0.090
4824.0–4835.0	−0.033	0.096
4899.0–4909.0	−0.108	0.115
4931.0–4942.0	−0.458	0.143
4975.0–4985.0	−0.159	0.086
5098.0–5108.0	−0.306	0.080
5141.0–5151.0	−0.387	0.085
5472.0–5482.0	+0.243	0.056
5707.0–5717.0	−0.056	0.085
6103.0–6113.0	−0.100	0.120
6172.0–6182.0	−0.499	0.156
[Ba/Fe]		
4551.0–4560.0	+0.303	0.045
4929.0–4939.0	+0.191	0.071
5849.0–5859.0	+0.274	0.085
6135.0–6145.0	+0.314	0.056

**Table A.8.** Individual abundance measurements for M33 H38

Wavelength [Å]	Value	Error
[Fe/H]		
4216.2–4276.6	−1.359	0.045
4267.0–4328.1	−0.656	0.040
4319.0–4380.9	...	
4372.3–4435.0	−0.746	0.035
4427.0–4490.4	−1.686	0.057
4483.0–4547.2	...	
4599.4–4665.3	−1.137	0.056
4659.9–4726.7	−1.127	0.056
4722.1–4789.8	−1.145	0.055
4785.8–4854.5	−1.055	0.070
4851.4–4920.9	−1.317	0.044
4918.7–4989.3	−1.150	0.045
4988.0–5059.6	−1.257	0.045
5059.3–5131.8	−1.019	0.041
5132.6–5206.2	−1.247	0.041
5208.0–5282.7	−1.206	0.035
5285.8–5361.6	−1.225	0.036
5365.8–5442.8	−1.240	0.036
5448.4–5526.5	−1.306	0.045
5533.5–5612.8	−1.386	0.041
5621.3–5701.9	−1.296	0.050
5712.0–5793.8	−1.167	0.066
5805.6–5888.8	−1.165	0.066
5902.4–5986.9	−1.368	0.060
6002.4–6088.4	−1.304	0.070
[Na/Fe]		
5677.0–5695.0	−0.020	0.096
6149.0–6166.0	+0.145	0.126
[Mg/Fe]		
4347.0–4357.0	...	
4565.0–4576.0	−0.498	0.145
4700.0–4707.0	+0.341	0.115
[Ca/Fe]		
4222.0–4232.0	−0.329	0.126
4280.0–4320.0	+0.650	0.120
4420.0–4430.0	+0.810	0.351
4432.0–4460.0	...	
4575.0–4591.0	−0.199	0.141
4873.0–4883.0	−0.273	0.300
5259.0–5268.0	+0.563	0.090
5580.0–5608.0	+0.810	0.066
6110.0–6171.0	+0.103	0.040
[Sc/Fe]		
4290.0–4328.0	...	
4350.0–4380.0	...	
4383.0–4435.0	...	
4665.0–4675.0	+0.210	0.316
5026.0–5036.0	−0.320	0.190
5638.0–5690.0	+0.001	0.066
[Ti/Fe]		
4292.0–4320.0	−0.349	0.126
4386.0–4420.0	+0.194	0.105
4440.0–4474.0	−0.428	0.080
4530.0–4542.0	−0.280	0.131
4545.0–4574.0	+0.740	0.035
4587.0–4593.0	−0.030	0.316
4650.0–4660.0	+0.121	0.180
4665.0–4715.0	+0.241	0.085
4750.0–4784.0	+0.220	0.101
4790.0–4850.0	+0.158	0.101

Table A.8. continued.

Wavelength [Å]	Value	Error
4993.0–5045.0	+0.379	0.051
5152.5–5160.0	+0.146	0.305
[Cr/Fe]		
4250.0–4270.0	−0.130	0.085
4272.0–4292.0	+0.019	0.154
4350.0–4375.0	...	
4375.0–4400.0	...	
4520.0–4547.0	−0.299	0.161
4547.0–4605.0	...	
4605.0–4660.0	−0.740	0.116
5235.0–5282.0	+0.349	0.056
5285.0–5330.0	−0.021	0.066
5342.0–5351.0	+0.070	0.115
5407.0–5413.0	−0.429	0.195
[Mn/Fe]		
4750.0–4780.0	−0.772	0.131
6010.0–6030.0	−0.413	0.116
[Ni/Fe]		
4600.0–4610.0	−0.649	0.350
4644.0–4654.0	−0.420	0.331
4681.0–4691.0	−0.071	0.236
4709.0–4719.0	−0.649	0.225
4824.0–4835.0	−0.081	0.191
4899.0–4909.0	−0.081	0.251
4931.0–4942.0	+0.659	0.175
4975.0–4985.0	−0.087	0.150
5075.0–5089.0	+0.241	0.094
5098.0–5108.0	+0.260	0.110
5141.0–5151.0	...	
5472.0–5482.0	+0.599	0.141
5707.0–5717.0	+0.736	0.240
[Ba/Fe]		
4551.0–4560.0	+0.680	0.021
4929.0–4939.0	−0.609	0.251
5849.0–5859.0	+0.279	0.185
6135.0–6145.0	+0.490	0.116

**Table A.9.** Individual abundance measurements for M33 M9

Wavelength [Å]	Value	Error
[Fe/H]		
4216.3–4276.7	−2.051	0.061
4267.1–4328.2	−1.721	0.071
4319.1–4381.0	−2.031	0.090
4372.4–4435.1	−1.630	0.041
4427.1–4490.5	−1.630	0.045
4483.1–4547.4	−1.831	0.051
4540.6–4605.7	−1.791	0.060
4599.5–4665.5	−1.801	0.051
4660.0–4726.8	−1.762	0.051
4722.2–4789.9	−1.682	0.061
4786.0–4854.6	−1.582	0.081
4851.5–4921.1	−1.701	0.036
4918.9–4989.4	−1.780	0.036
4988.1–5059.7	−1.901	0.030
5059.4–5132.0	−1.611	0.030
5132.7–5206.3	−1.801	0.030
5208.2–5282.9	−1.601	0.025
5285.9–5361.7	−1.780	0.036
5366.0–5442.9	−1.762	0.026
5448.5–5526.6	−1.801	0.041
5533.7–5613.0	−1.701	0.030
5621.5–5702.0	−1.772	0.040
5712.1–5794.0	−1.762	0.066
5805.8–5888.9	−1.911	0.096
5902.5–5987.0	−1.682	0.060
6002.6–6088.5	−1.640	0.051
[Na/Fe]		
5677.0–5695.0	+0.207	0.081
6149.0–6166.0	−0.121	0.386
[Mg/Fe]		
4347.0–4357.0	−0.333	0.181
4565.0–4576.0	−0.182	0.150
4700.0–4707.0	+0.089	0.085
[Ca/Fe]		
4222.0–4232.0	−0.282	0.105
4280.0–4320.0	+0.138	0.110
4420.0–4430.0	+0.658	0.226
4432.0–4460.0	+0.147	0.080
4575.0–4591.0	−0.121	0.105
4873.0–4883.0	+0.447	0.215
5259.0–5268.0	+0.338	0.066
5580.0–5608.0	+0.418	0.045
6110.0–6171.0	+0.277	0.035
[Sc/Fe]		
4290.0–4328.0	+0.008	0.131
4350.0–4380.0	−0.023	0.200
4383.0–4435.0	−0.302	0.145
4665.0–4675.0	−0.542	0.310
5026.0–5036.0	−0.162	0.110
5638.0–5690.0	+0.288	0.056
[Ti/Fe]		
4292.0–4320.0	+0.198	0.091
4386.0–4420.0	+0.228	0.066
4440.0–4474.0	+0.578	0.051
4530.0–4542.0	+0.277	0.080
4545.0–4574.0	+0.418	0.070
4587.0–4593.0	+0.768	0.136
4650.0–4660.0	−0.131	0.185
4665.0–4715.0	+0.198	0.075
4750.0–4784.0	+0.357	0.081

Table A.9. continued.

Wavelength [Å]	Value	Error
4790.0–4850.0	+0.259	0.085
4993.0–5045.0	+0.338	0.045
5152.5–5160.0	+0.118	0.206
[Cr/Fe]		
4250.0–4270.0	...	
4272.0–4292.0	−0.243	0.191
4350.0–4375.0	−0.221	0.150
4375.0–4400.0	...	
4520.0–4547.0	−0.111	0.120
4547.0–4605.0	+0.048	0.075
4605.0–4660.0	−0.092	0.070
5235.0–5282.0	+0.008	0.060
5285.0–5330.0	+0.008	0.051
5342.0–5351.0	+0.048	0.105
5407.0–5413.0	−0.441	0.136
[Mn/Fe]		
4750.0–4780.0	−0.341	0.075
6010.0–6030.0	−0.732	0.235
[Ni/Fe]		
4600.0–4610.0	+0.687	0.141
4644.0–4654.0	−0.033	0.191
4681.0–4691.0	−0.002	0.266
4709.0–4719.0	+0.208	0.115
4824.0–4835.0	+0.318	0.126
4899.0–4909.0	+0.028	0.146
4931.0–4942.0	−0.622	0.555
4975.0–4985.0	−0.302	0.146
5075.0–5089.0	−0.072	0.085
5098.0–5108.0	−0.323	0.161
5141.0–5151.0	−0.162	0.160
5472.0–5482.0	+0.198	0.105
5707.0–5717.0	...	
[Ba/Fe]		
4551.0–4560.0	...	
4929.0–4939.0	+0.319	0.115
5849.0–5859.0	+0.578	0.110
6135.0–6145.0	+0.668	0.060



**Table A.10.** Individual abundance measurements for M33 R12

Wavelength [Å]	Value	Error
[Fe/H]		
4215.9–4276.3	−1.060	0.030
4266.7–4327.8	−0.989	0.036
4318.7–4380.6	−0.840	0.041
4372.0–4434.6	−0.960	0.026
4426.6–4490.1	−0.931	0.030
4482.7–4546.9	−0.820	0.030
4540.1–4605.2	−1.040	0.030
4599.1–4665.0	−1.016	0.026
4659.6–4726.4	−1.008	0.025
4721.7–4789.4	−0.778	0.030
4785.5–4854.1	−1.040	0.040
4851.0–4920.6	−0.900	0.016
4918.4–4988.9	−0.891	0.016
4987.6–5059.2	−0.970	0.016
5058.9–5131.4	−0.941	0.020
5132.2–5205.8	−1.081	0.017
5207.7–5282.3	−0.860	0.015
5285.4–5361.1	−0.939	0.021
5365.4–5442.4	−0.991	0.016
5448.0–5526.1	−0.993	0.021
5533.1–5612.4	−0.961	0.021
5620.9–5701.5	−0.950	0.020
5711.6–5793.4	−0.919	0.030
5805.2–5888.3	−1.011	0.036
5901.9–5986.5	−0.810	0.026
6002.0–6087.9	−0.758	0.026
[Na/Fe]		
5677.0–5695.0	+0.098	0.041
6149.0–6166.0	+0.152	0.062
[Mg/Fe]		
4347.0–4357.0	+0.458	0.150
4565.0–4576.0	+0.230	0.080
4700.0–4707.0	+0.160	0.056
[Ca/Fe]		
4222.0–4232.0	+0.332	0.066
4280.0–4320.0	+0.403	0.081
4420.0–4430.0	+0.733	0.146
4432.0–4460.0	+0.244	0.045
4575.0–4591.0	+0.168	0.056
4873.0–4883.0	+0.671	0.186
5259.0–5268.0	+0.544	0.045
5580.0–5608.0	+0.403	0.030
6110.0–6171.0	+0.162	0.021
[Sc/Fe]		
4290.0–4328.0	+0.002	0.115
4350.0–4380.0	+0.116	0.155
4383.0–4435.0	+0.193	0.101
4665.0–4675.0	−0.317	0.190
5026.0–5036.0	−0.230	0.075
5638.0–5690.0	+0.151	0.030
[Ti/Fe]		
4292.0–4320.0	+0.162	0.066
4386.0–4420.0	+0.373	0.040
4440.0–4474.0	+0.052	0.046
4530.0–4542.0	+0.034	0.066
4545.0–4574.0	+0.472	0.036
4587.0–4593.0	+0.244	0.110
4650.0–4660.0	+0.125	0.080
4665.0–4715.0	+0.103	0.041
4750.0–4784.0	+0.133	0.045

Table A.10. continued.

Wavelength [Å]	Value	Error
4790.0–4850.0	+0.394	0.040
4993.0–5045.0	+0.283	0.026
5152.5–5160.0	+0.625	0.141
[Cr/Fe]		
4250.0–4270.0	−0.537	0.096
4272.0–4292.0	+0.073	0.061
4350.0–4375.0	+0.193	0.101
4375.0–4400.0	−0.447	0.151
4520.0–4547.0	−0.195	0.066
4547.0–4605.0	+0.024	0.045
4605.0–4660.0	+0.103	0.038
5235.0–5282.0	+0.183	0.030
5285.0–5330.0	+0.012	0.030
5342.0–5351.0	−0.206	0.061
5407.0–5413.0	−0.115	0.083
[Mn/Fe]		
4750.0–4780.0	−0.266	0.046
6010.0–6030.0	−0.126	0.061
[Ni/Fe]		
4600.0–4610.0	−0.127	0.075
4644.0–4654.0	−0.596	0.136
4681.0–4691.0	+0.105	0.096
4709.0–4719.0	+0.043	0.075
4824.0–4835.0	+0.068	0.080
4899.0–4909.0	+0.043	0.120
4931.0–4942.0	−0.260	0.115
4975.0–4985.0	+0.083	0.066
5075.0–5089.0	+0.002	0.045
5098.0–5108.0	+0.217	0.055
5141.0–5151.0	+0.281	0.116
5472.0–5482.0	+0.352	0.058
5707.0–5717.0	−0.337	0.146
[Ba/Fe]		
4551.0–4560.0	+0.004	0.091
4929.0–4939.0	+0.380	0.085
5849.0–5859.0	+0.533	0.090
6135.0–6145.0	+0.466	0.045

**Table A.11.** Individual abundance measurements for M33 U49

Wavelength [Å]	Value	Error
[Fe/H]		
4214.9–4275.3	−1.457	0.051
4265.7–4326.8	−1.908	0.080
4317.7–4379.6	−1.727	0.108
4371.0–4433.6	−1.387	0.036
4425.6–4489.1	−1.317	0.056
4481.6–4545.9	−1.422	0.075
4539.1–4604.1	−1.388	0.071
4598.0–4663.9	−1.438	0.066
4658.5–4725.3	−1.916	0.081
4720.6–4788.3	−1.487	0.081
4784.4–4853.0	−1.306	0.085
4849.9–4919.4	−1.558	0.042
4917.3–4987.8	−1.378	0.040
4986.5–5058.0	−1.438	0.041
5057.7–5130.2	−1.248	0.041
5131.0–5204.6	−1.618	0.045
5206.5–5281.1	−1.457	0.041
5284.2–5359.9	−1.388	0.041
5364.2–5441.1	−1.542	0.035
5446.7–5524.8	−1.409	0.051
5531.8–5611.1	−1.469	0.041
5619.6–5700.2	−1.486	0.045
5710.3–5792.1	−1.146	0.060
5803.9–5887.0	−1.468	0.090
5900.6–5985.1	−1.317	0.056
6000.6–6086.5	−1.516	0.070
[Na/Fe]		
5677.0–5693.0	+0.057	0.115
6149.0–6166.0	+0.187	0.168
[Mg/Fe]		
4347.0–4357.0	−0.281	0.405
4565.0–4576.0	+0.279	0.201
4700.0–4707.0	+0.322	0.136
[Ca/Fe]		
4222.0–4232.0	−0.511	0.136
4280.0–4320.0	+0.273	0.116
4420.0–4430.0	+0.521	0.261
4432.0–4460.0	−0.442	0.135
4575.0–4591.0	−0.129	0.126
4873.0–4883.0	...	
5259.0–5268.0	+0.860	0.096
5580.0–5608.0	+0.260	0.060
6110.0–6171.0	+0.246	0.056
[Sc/Fe]		
4290.0–4328.0	−0.571	0.210
4350.0–4380.0	+0.469	0.201
4383.0–4435.0	...	
4665.0–4675.0	−0.102	0.261
5026.0–5036.0	+0.425	0.126
5638.0–5690.0	+0.288	0.061
[Ti/Fe]		
4292.0–4320.0	+0.390	0.100
4386.0–4420.0	+0.519	0.081
4440.0–4474.0	+0.378	0.070
4530.0–4542.0	−0.480	0.145
4545.0–4574.0	−0.082	0.100
4587.0–4593.0	...	
4650.0–4660.0	+0.369	0.136
4665.0–4715.0	+0.279	0.095
4750.0–4784.0	+0.738	0.091

Table A.11. continued.

Wavelength [Å]	Value	Error
4790.0–4850.0	+0.392	0.105
4993.0–5045.0	+0.482	0.051
5152.5–5160.0	−0.060	0.286
[Cr/Fe]		
4250.0–4270.0	−0.420	0.146
4272.0–4292.0	...	
4350.0–4375.0	+0.049	0.180
4375.0–4400.0	+0.833	0.201
4520.0–4547.0	−0.427	0.191
4547.0–4605.0	+0.459	0.071
4605.0–4660.0	+0.110	0.081
5235.0–5282.0	+0.169	0.071
5285.0–5330.0	−0.195	0.085
5342.0–5351.0	−0.160	0.145
5407.0–5413.0	+0.008	0.166
[Mn/Fe]		
4750.0–4780.0	+0.049	0.071
6010.0–6030.0	−0.283	0.135
[Ni/Fe]		
4600.0–4610.0	+0.340	0.159
4644.0–4654.0	...	
4681.0–4691.0	...	
4709.0–4719.0	−0.442	0.221
4824.0–4835.0	+0.308	0.146
4899.0–4909.0	−0.498	0.381
4931.0–4942.0	−0.027	0.225
4975.0–4985.0	+0.089	0.150
5075.0–5089.0	−0.245	0.136
5098.0–5108.0	+0.018	0.150
5141.0–5151.0	−0.760	0.270
5472.0–5482.0	+0.620	0.101
5707.0–5717.0	...	
[Ba/Fe]		
4551.0–4560.0	−0.801	0.276
4929.0–4939.0	+0.321	0.160
5849.0–5859.0	...	
6135.0–6145.0	+0.740	0.085

**Table A.12.** Individual abundance measurements for the WLM GC

Wavelength [Å]	Value	Error
[Fe/H]		
4200.0–4400.0	−1.820	0.015
4400.0–4600.0	−1.921	0.015
4600.0–4800.0	−2.001	0.021
4800.0–5000.0	−2.061	0.015
5000.0–5150.0	−1.921	0.015
5250.0–5400.0	−1.842	0.026
5400.0–5600.0	−2.061	0.026
5600.0–5800.0	−2.051	0.036
5800.0–6000.0	−2.032	0.061
6000.0–6200.0	−1.910	0.041
[Na/Fe]		
5677.0–5695.0	+0.217	0.141
6149.0–6166.0	+0.277	0.431
[Mg/Fe]		
4347.0–4357.0	−0.183	0.170
4565.0–4576.0	+0.076	0.110
4700.0–4707.0	+0.166	0.075
5523.0–5531.5	−0.124	0.115
5705.0–5715.0	+0.095	0.175
[Ca/Fe]		
4420.0–4460.0	+0.146	0.051
4575.0–4591.0	−0.004	0.085
4873.0–4883.0	+0.496	0.120
5259.0–5268.0	+0.447	0.096
5580.0–5610.0	+0.357	0.051
6100.0–6175.0	+0.207	0.036
[Sc/Fe]		
4290.0–4330.0	+0.467	0.071
4350.0–4440.0	+0.207	0.071
4665.0–4675.0	−0.005	0.120
5026.0–5036.0	+0.056	0.136
5521.0–5531.0	−0.233	0.195
5638.0–5690.0	+0.135	0.075
[Ti/Fe]		
4292.0–4320.0	−0.444	0.075
4386.0–4420.0	+0.176	0.051
4440.0–4474.0	+0.225	0.051
4532.0–4574.0	+0.305	0.030
4587.0–4593.0	+0.437	0.085
4650.0–4715.0	+0.217	0.051
4750.0–4850.0	+0.176	0.056
4980.0–5045.0	+0.095	0.030
5152.5–5160.0	+0.095	0.115
[Cr/Fe]		
4250.0–4292.0	−0.403	0.081
4350.0–4400.0	−0.615	0.145
4520.0–4660.0	−0.063	0.040
5235.0–5330.0	+0.026	0.061
5342.0–5351.0	−0.413	0.166
5407.0–5413.0	+0.175	0.145
[Mn/Fe]		
4750.0–4790.0	−0.503	0.070
6010.0–6030.0	−0.233	0.206
[Ni/Fe]		
4600.0–4610.0	−0.124	0.201
4644.0–4654.0	+0.015	0.145
4681.0–4691.0	+0.066	0.266
4709.0–4719.0	−0.354	0.136
4824.0–4835.0	< −0.455	
4899.0–4909.0	−0.104	0.185

**Table A.12.** continued.

Wavelength [Å]	Value	Error
4931.0–4942.0	−0.214	0.290
4975.0–4985.0	+0.105	0.085
5075.0–5089.0	−0.144	0.081
5098.0–5108.0	−0.273	0.175
5141.0–5151.0	−0.904	0.611
5472.0–5482.0	...	
5707.0–5717.0	−0.253	0.165
6103.0–6113.0	+0.296	0.126
6172.0–6182.0	...	
[Ba/Fe]		
4551.0–4560.0	+0.227	0.081
4929.0–4939.0	−0.114	0.091
5849.0–5859.0	−0.084	0.215
6135.0–6145.0	+0.257	0.126

**Table A.13.** Individual abundance measurements for Fornax 3

Wavelength [Å]	Value	Error
[Fe/H]		
4200.0–4400.0	−2.391	0.010
4400.0–4600.0	−2.401	0.011
4600.0–4800.0	−2.401	0.021
4800.0–5000.0	−2.372	0.011
5000.0–5150.0	−2.272	0.011
5250.0–5400.0	−2.311	0.016
5400.0–5600.0	−2.331	0.016
5600.0–5800.0	−2.482	0.026
5800.0–6000.0	−2.531	0.096
6000.0–6200.0	−2.182	0.026
[Na/Fe]		
5677.0–5695.0	+0.013	0.171
6149.0–6166.0	...	
[Mg/Fe]		
4347.0–4357.0	−0.158	0.085
4565.0–4576.0	+0.042	0.075
4700.0–4707.0	−0.178	0.056
5523.0–5531.5	+0.092	0.060
5705.0–5715.0	+0.342	0.105
[Ca/Fe]		
4222.0–4232.0	+0.022	0.041
4280.0–4320.0	+0.132	0.035
4420.0–4460.0	+0.203	0.025
4575.0–4591.0	−0.278	0.126
4873.0–4883.0	+0.762	0.066
5259.0–5268.0	+0.302	0.061
5580.0–5610.0	+0.142	0.040
6100.0–6175.0	+0.342	0.020
[Sc/Fe]		
4290.0–4330.0	+0.122	0.051
4350.0–4440.0	+0.323	0.041
4665.0–4675.0	−0.297	0.120
5026.0–5036.0	−0.248	0.090
5521.0–5531.0	+0.221	0.085
5638.0–5690.0	+0.262	0.055
[Ti/Fe]		
4292.0–4320.0	+0.273	0.030
4386.0–4420.0	+0.452	0.025
4440.0–4474.0	+0.332	0.030
4532.0–4574.0	+0.291	0.020
4587.0–4593.0	+0.452	0.056
4650.0–4715.0	+0.312	0.041
4750.0–4850.0	+0.432	0.030
4980.0–5045.0	+0.161	0.020
5152.5–5160.0	+0.232	0.081
[Cr/Fe]		
4250.0–4292.0	−0.257	0.040
4350.0–4400.0	−0.327	0.075
4520.0–4660.0	−0.188	0.036
5235.0–5330.0	−0.177	0.056
5342.0–5351.0	+0.061	0.070
5407.0–5413.0	−0.127	0.085
[Mn/Fe]		
4750.0–4790.0	−0.518	0.070
6010.0–6030.0	−0.127	0.180
[Ni/Fe]		
4600.0–4610.0	...	
4644.0–4654.0	−0.528	0.346
4681.0–4691.0	+0.342	0.151
4709.0–4719.0	−0.408	0.120

**Table A.13.** continued.

Wavelength [Å]	Value	Error
4824.0–4835.0	+0.132	0.126
4899.0–4909.0	−0.358	0.295
4931.0–4942.0	...	
4975.0–4985.0	−0.207	0.101
5075.0–5089.0	−0.358	0.101
5098.0–5108.0	−0.088	0.146
5141.0–5151.0	−0.207	0.131
5472.0–5482.0	+0.262	0.066
5707.0–5717.0	+0.132	0.091
6103.0–6113.0	−0.129	0.175
6172.0–6182.0	−0.048	0.515
[Ba/Fe]		
4551.0–4560.0	...	
4929.0–4939.0	+0.523	0.040
5849.0–5859.0	+0.433	0.080
6135.0–6145.0	+0.692	0.061



**Table A.14.** Individual abundance measurements for Fornax 4

Wavelength [Å]	Value	Error
[Fe/H]		
4200.0–4400.0	−1.413	0.011
4400.0–4600.0	−1.442	0.005
4600.0–4800.0	−1.382	0.005
4800.0–5000.0	−1.421	0.005
5000.0–5150.0	−1.352	0.005
5250.0–5400.0	−1.352	0.011
5400.0–5600.0	−1.352	0.011
5600.0–5800.0	−1.352	0.011
5800.0–6000.0	−1.362	0.020
6000.0–6200.0	−1.242	0.011
[Na/Fe]		
5677.0–5695.0	−0.177	0.045
6149.0–6166.0	−0.258	0.120
[Mg/Fe]		
4347.0–4357.0	−0.507	0.080
4565.0–4576.0	−0.188	0.066
4700.0–4707.0	+0.112	0.035
5523.0–5531.5	+0.132	0.051
5705.0–5715.0	−0.108	0.051
[Ca/Fe]		
4222.0–4232.0	−0.168	0.030
4280.0–4320.0	+0.173	0.041
4420.0–4460.0	+0.002	0.021
4575.0–4591.0	−0.068	0.041
4873.0–4883.0	+0.591	0.075
5259.0–5268.0	+0.222	0.040
5580.0–5610.0	+0.173	0.020
6100.0–6175.0	+0.083	0.015
[Sc/Fe]		
4290.0–4330.0	+0.102	0.045
4350.0–4440.0	−0.068	0.035
4665.0–4675.0	−0.287	0.075
5026.0–5036.0	−0.088	0.040
5521.0–5531.0	−0.197	0.070
5638.0–5690.0	−0.107	0.036
[Ti/Fe]		
4292.0–4320.0	+0.042	0.030
4386.0–4420.0	+0.312	0.021
4440.0–4474.0	+0.072	0.021
4532.0–4574.0	+0.103	0.015
4587.0–4593.0	+0.312	0.051
4650.0–4715.0	−0.008	0.025
4750.0–4850.0	+0.163	0.020
4980.0–5045.0	+0.083	0.015
5152.5–5160.0	+0.242	0.055
[Cr/Fe]		
4250.0–4292.0	−0.117	0.030
4350.0–4400.0	−0.388	0.051
4520.0–4660.0	−0.107	0.016
5235.0–5330.0	−0.038	0.021
5342.0–5351.0	+0.122	0.051
5407.0–5413.0	−0.038	0.070
[Mn/Fe]		
4750.0–4790.0	−0.337	0.025
6010.0–6030.0	−0.467	0.051
[Ni/Fe]		
4600.0–4610.0	−0.239	0.061
4644.0–4654.0	−0.427	0.091
4681.0–4691.0	−0.339	0.085
4709.0–4719.0	−0.217	0.051

**Table A.14.** continued.

Wavelength [Å]	Value	Error
4824.0–4835.0	−0.008	0.056
4899.0–4909.0	−0.149	0.055
4931.0–4942.0	−0.468	0.075
4975.0–4985.0	−0.268	0.041
5075.0–5089.0	−0.149	0.026
5098.0–5108.0	−0.249	0.045
5141.0–5151.0	−0.388	0.041
5472.0–5482.0	+0.083	0.066
5707.0–5717.0	+0.051	0.046
6103.0–6113.0	+0.103	0.055
6172.0–6182.0	−0.348	0.085
[Ba/Fe]		
4551.0–4560.0	+0.323	0.030
4929.0–4939.0	+0.273	0.041
5849.0–5859.0	+0.181	0.081
6135.0–6145.0	+0.171	0.051

**Table A.15.** Individual abundance measurements for Fornax 5

Wavelength [Å]	Value	Error
[Fe/H]		
4200.0–4400.0	−2.071	0.016
4400.0–4600.0	−2.171	0.020
4600.0–4800.0	−2.150	0.025
4800.0–5000.0	−2.191	0.021
5000.0–5150.0	−2.171	0.010
5250.0–5400.0	−2.052	0.020
5400.0–5600.0	−2.191	0.021
5600.0–5800.0	−2.042	0.035
5800.0–6000.0	−1.991	0.056
6000.0–6200.0	−1.911	0.030
[Na/Fe]		
5677.0–5695.0	+0.484	0.096
6149.0–6166.0	...	
[Mg/Fe]		
4347.0–4357.0	+0.313	0.115
4565.0–4576.0	+0.453	0.105
4700.0–4707.0	+0.143	0.070
5523.0–5531.5	−0.018	0.101
5705.0–5715.0	+0.274	0.136
[Ca/Fe]		
4222.0–4232.0	+0.114	0.060
4280.0–4320.0	+0.343	0.051
4420.0–4460.0	+0.053	0.051
4575.0–4591.0	−0.277	0.150
4873.0–4883.0	+0.722	0.085
5259.0–5268.0	+0.443	0.080
5580.0–5610.0	+0.363	0.051
6100.0–6175.0	+0.274	0.036
[Sc/Fe]		
4290.0–4330.0	+0.143	0.071
4350.0–4440.0	+0.042	0.066
4665.0–4675.0	−0.626	0.191
5026.0–5036.0	−0.827	0.165
5521.0–5531.0	−0.247	0.166
5638.0–5690.0	+0.174	0.081
[Ti/Fe]		
4292.0–4320.0	+0.274	0.051
4386.0–4420.0	+0.353	0.045
4440.0–4474.0	+0.263	0.051
4532.0–4574.0	+0.343	0.036
4587.0–4593.0	+0.433	0.081
4650.0–4715.0	+0.184	0.060
4750.0–4850.0	+0.363	0.045
4980.0–5045.0	+0.162	0.026
5152.5–5160.0	+0.223	0.096
[Cr/Fe]		
4250.0–4292.0	+0.294	0.065
4350.0–4400.0	−0.517	0.136
4520.0–4660.0	+0.052	0.036
5235.0–5330.0	−0.057	0.066
5342.0–5351.0	+0.294	0.096
5407.0–5413.0	−0.266	0.136
[Mn/Fe]		
4750.0–4790.0	−0.367	0.066
6010.0–6030.0	...	
[Ni/Fe]		
4600.0–4610.0	...	
4644.0–4654.0	−0.587	0.520
4681.0–4691.0	+0.303	0.201
4709.0–4719.0	−0.267	0.126

**Table A.15.** continued.

Wavelength [Å]	Value	Error
4824.0–4835.0	−0.186	0.261
4899.0–4909.0	+0.204	0.096
4931.0–4942.0	+0.133	0.196
4975.0–4985.0	+0.033	0.090
5075.0–5089.0	−0.067	0.071
5098.0–5108.0	−0.336	0.180
5141.0–5151.0	+0.124	0.096
5472.0–5482.0	−0.336	0.166
5707.0–5717.0	+0.013	0.131
6103.0–6113.0	+0.233	0.126
6172.0–6182.0	+0.574	0.126
[Ba/Fe]		
4551.0–4560.0	+0.133	0.080
4929.0–4939.0	−0.017	0.070
5849.0–5859.0	−0.017	0.136
6135.0–6145.0	−0.266	0.120